AGU PUBLICATIONS

JGR

Journal of Geophysical Research: Solid Earth

RESEARCH ARTICLE
10.1002/2014JB011631

Key Points:
- Brine affects chalk chemistry and solid volume is not conserved
- Integrating compaction and nonequilibrium water flood
- Porosity and permeability affected by mechanical compaction and chemical effects

Correspondence to:
A. Nermoen,
anders.nermoen@iris.no

Citation:
Nermoen, A., R. I. Korsnes, A. Hiorth, and M. V. Madland (2015), Porosity and permeability development in compacting chalks during flooding of nonequilibrium brines: Insights from long-term experiment, *J. Geophys. Res. Solid Earth*, *120*, 2935–2960, doi:10.1002/2014JB011631.

Received 24 SEP 2014
Accepted 26 MAR 2015
Accepted article online 31 MAR 2015
Published online 5 MAY 2015

Porosity and permeability development in compacting chalks during flooding of nonequilibrium brines: Insights from long-term experiment

Anders Nermoen[1,2], Reidar I. Korsnes[2,3], Aksel Hiorth[1,2,3], and Merete V. Madland[2,3]

[1]IRIS AS - International Research Institute of Stavanger, Stavanger, Norway, [2]National IOR Centre of Norway, Stavanger, Norway, [3]Department of Petroleum Technology, University of Stavanger, Stavanger, Norway

Abstract We report the complete chemical alteration of a Liège outcrop chalk core resulting from a 1072 flow-through experiment performed during mechanical compaction at 130°C. Chemical rock-fluid interactions alter the volumetric strain, porosity, and permeability in a nontrivial way. The porosity reduced only from 41.32% to 40.14%, even though the plug compacted more than 25%. We present a novel analysis of the experimental data, which demonstrates that the geochemical alteration does not conserve the volume of the solids, and therefore, the strain is partitioned additively into a pore volume and solid volume component. At stresses beyond yield, the observed deformation can be explained by grain reorganization reducing the pore space between grains and solid volume changes from the rock-fluid interactions. The mechanical and chemical effects are discussed in relation to the observed permeability development.

1. Introduction

The physiochemical interplay between the flow of fluids within deformable, reactive granular porous materials (consisting of solids and voids) is of great importance in Earth sciences in the study, e.g., of long-term creep behavior of crustal rocks, and to industrial applications such as CO_2 sequestration [*Emberley et al.,* 2005], ore deposits [*Cathles*, 1981], radioactive waste disposal, hydrology, hydrocarbon migration, and reservoir engineering [*Megawati et al.,* 2012; *Nagel*, 2001] as well as chemical and pharmaceutical industries [*Durand*, 1997]. Reactive pore fluids, in nonequilibrium with the rocks, lead to dissolution and precipitation that transform one mineral into another thereby affecting the grain texture and morphology, the material strength, and the fluid pathways that may evolve through time and space.

The mechanical integrity of reservoir chalks during water flooding has been of significant interest in the scientific and industrial communities since the seabed subsidence at Ekofisk was discovered [*Doornhof et al.,* 2006; *Hermansen et al.,* 1997; *Kristiansen et al.,* 2005]. During primary production, the pore pressure was lowered increasing the effective stress in the reservoir as pressurized fluids carry some of the weight from the overburden rocks [*Terzaghi*, 1923; *Nur and Byerlee,* 1971; *Omdal et al.,* 2009; *Nermoen et al.,* 2013]. At the Ekofisk field, the primary production phase led to compaction in the overburden and the reservoir and corresponding seafloor subsidence with detrimental effects to the platforms resting on the seafloor and to the production equipment [*Nagel*, 2001]. In addition, the fluid pressure reduction led to a significant decline in production rates during the last years of the 1970s and the first half of the 1980s [*Hermansen et al.,* 1997]. During this period, the compaction rate was ~35 cm/yr [*Doornhof et al.,* 2006]. After seawater injection started, it took ~4 years before the reservoir pressure increased (re-pressurized). As a consequence, the compaction rate reduced to ~1/3 in the reservoir volumes in contact with the injected seawater [*Amyx et al.,* 1960; *Jensen et al.,* 2000; *Awan et al.,* 2008; *Spencer et al.,* 2008].

The prevailing compaction and seafloor subsidence after re-pressurization indicate that it is not only the stress and pressure level that control the rates of deformation. This field observation is supported by decades of experimental work showing how the chemical composition of the pore fluid plays a role in the mechanical behavior of chalks. For example, the stress level where irreversible pore collapse and compaction (in *p-q* space) occur is reduced by seawater and other brines containing, e.g., sulfate ions [see, e.g., *Megawati et al.*, 2012; *Liteanu and Spiers*, 2009; *Liteanu et al.*, 2013; *Omdal*, 2010; *Korsnes et al.*, 2008a; *Madland et al.*, 2002; *Heggheim et al.*, 2005; *Risnes et al.*, 2005]. For chalks, the rate of deformation at constant stress level (i.e., the creep rate) is also affected by the composition of injected fluids and brines

[e.g., *Hellmann et al.*, 2002b, 2002a; *Madland et al.*, 2006; *Risnes*, 2001; *Korsnes et al.*, 2008a; *Risnes et al.*, 2003; *Grgic*, 2011; *Neveux et al.*, 2014a, 2014b]. A similar phenomenon can also be seen in subcritical crack growth experiments where cracks may propagate even at imposed stresses below a critical level because of the chemical interplay between the fluids and the rock surfaces close to the crack tip [*Røyne et al.,* 2011]. As such, the presence of fluids may in some cases drive deformation at stresses lower than the critical level.

Several authors have claimed that by changing the injected water chemistry, oil could be recovered more efficiently, both because of favorable changes in the wetting condition and changes to the compaction rate [*Amyx et al.,* 1960; *Hermansen et al.,* 2000].

The chemical impact on the mechanical strength of a porous material is multifaceted as both time-dependent and time-independent processes play a role. Dissolution-precipitation kinetics induce time-dependent chemical changes to both the mineral constituency and the solid volume in a porous body [*Ehrenberg et al.,* 2012; *Ruiz-Agudo et al.,* 2014]. The chemical potential (μ), related to Gibbs energy of formation via $G = \mu N$, governs the chemical stability of minerals at the rock-fluid interface. The state variables for the Gibbs energy are temperature and pressure. In granular systems, stress changes induce significant spatial variations in local stress levels. The difference between stresses at solid-solid contacts and the external force applied over the bulk area of a chalk plug can be significant. The Biot coefficient, which relates the pore pressure to the effective stress estimate, is linked to the consolidated area across grain contacts (see, e.g., *Nermoen et al.* [2013] for a discussion). In the case of chalks, with a Biot coefficient on the order of 0.65–1.0 [see, e.g., *Vasquez et al.,* 2009; *Alam et al.,* 2012; [*Nermoen et al.,* 2013; *Omdal et al.,* 2009], this leads to a significant increase in the normal stresses at grain contacts, possibly up to 10–20 times the effective stress. Regardless of which local thermodynamic pressures have relevance for the local chemical potential at the grain contacts—either pore pressure in the lower end or contact stresses in the upper—these spatial stress differences may lead to varied solubility within the porous rocks. The additional dissolution at grain contacts is termed pressure solution (see, e.g., *Croize et al.* [2013] for a review). *Croize et al.* [2010] reported indenter experiments on calcite crystals and showed that measurable pressure solution occurred at stresses above approximately 400 MPa.

Pressure solution has been suggested as a drive mechanism to explain the prevailing time-dependent creep observed in other long-term experiments. An example is described in *Hellmann et al.* [2002b, 2002a] in which a chalk core was compacted for almost 700 days. Any pressure solution would add to the $CaCO_3$ dissolution triggered by precipitation of Mg-bearing minerals which is expected from equilibrium calculations reported in, e.g., *Hiorth et al.* [2013], *Hiorth et al.* [2010], *Madland et al.* [2011], and *Cathles* [2006].

Not only does dissolution-precipitation arising from the nonequilibrium nature of the rock-fluid interface affect the total volumetric deformation, but ion adsorption onto charged chalk surfaces also sets up electrostatic potentials in the diffusive double layer. These potentials induce disjoining pressures in the intergranular contacts altering the adhesive van der Waal forces [*Megawati et al.*, 2012]. The adsorption onto available surface sites may reduce internal friction, allowing grains to more easily slide and reorganize, leading to (1) additional rates of compaction [*Nermoen et al.,* 2014] and (2) yielding at lower effective stresses than would be the case if the pores were dry, filled with oil or brines not containing these surface active ions [*Liteanu et al.,* 2013; *Korsnes et al.,* 2008a]. The increased movement of solid-solid surfaces relative to each other caused by surface chemistry processes reduces the volume of the voids, i.e., the porosity. The experimental evidence between material strength and physiochemical surface effects dates back to experiments performed in the 1920s by P. A. Rehbinder [*Andrade et al.*, 1950]. Rehbinder showed that surface active agents (or any molecules reducing the surface energy of a solid, typically water molecules on ionic and ionic-covalent crystal matter) assist externally applied loads in deforming or fracturing the material [*Rehbinder and Shchukin,* 1972; *Traskin*, 2009]. Based on this line of argument, we surmise that chemically induced compaction has both a time-dependent component (as it takes time for dissolution and precipitation to change the volume of solids) and a time-independent component that occurs faster (from the disjoining pressure that induces additional compaction by rapid reduction of the pore volume). As the two proposed water-weakening mechanisms change the solid volume and pore volume, respectively, they lead to completely different consequences to the dynamic porosity development during mechanical compaction and flooding of nonequilibrium brines.

The void fraction and flow properties are important for reservoir engineers to provide estimates of the total resource potential in a hydrocarbon field—the void fraction is where hydrocarbons are trapped and may flow. The flow field in a reservoir depends upon the permeability. The permeability describes the relation

between the flow rate and the pressure gradient [*Shafer et al.,* 2012]. There is a link between the porosity and the mechanical behavior of chalks [e.g., *Engstrøm*, 1992] and between the porosity and permeability. We will study the perm-porosity link in this paper by comparing the estimated porosity evolution through time and the measured permeability. The permeability also depends on several other material parameters that may change during compaction and dissolution/precipitation. Examples include the specific surface area (S), the distribution of pore throat diameters, pore size distribution, the tortuosity (τ), the relative permeability arising from capillary forces introduced by surface tension (γ) in the presence of other fluids, and the hydrophobic/hydrophilic (wettability) properties of the mineral surfaces. Several of these factors are interdependent, and their importance to the flow arises from details of the mineral composition and morphology on submicron scale [*Feder*, 1996; *Amyx et al.,* 1960]. As nonequilibrium fluids are injected into chalks, this leads to dissolution and precipitation reactions changing several of the factors above.

Clearly, there is potential to enhance oil production by changing the water chemistry, although translating the effect of water chemistry on oil recovery from core to field scale is highly nontrivial. It requires models that take rock-fluid interactions and their effect on the flow of oil and water into account. However, these models need to be calibrated to core data, preferentially through experiments performed in realistic conditions and at times comparable to those in a producing oil reservoir. In this study, the focus is on the time-dependent behavior of Darcy-scale parameters such as permeability, porosity, and creep strain of a chalk plug that was first flooded with NaCl brine for 7 days (which is more or less inert to the chalk surface), and thereafter $MgCl_2$ brine (with changing injection rates). The test was performed at 130°C and at effective stress of 10.4 MPa for 1072 days.

Although previous studies have investigated the effect of nonequilibrium brines into porous rocks and the corresponding compaction process over significant time intervals (such as *Hellmann et al.* [2002a, 2002b]), this is the only study—that we know of—which measured compaction, permeability, porosity, and ion composition of the effluent brine over such a long time period. Furthermore, we present scanning electron microscopy (SEM) and energy dispersive spectroscopy (EDS) observations of the mineral assemblage where the primary mineral calcite (calcium carbonate) has been almost completely transformed to a magnesium bearing carbonate.

We do not believe that the brines used in this paper are optimal Enhanced Oil Recovery (EOR) fluids for chalk or carbonate fields, but Mg^{2+} is one of the major surface active cations in seawater used in chalk fields. In order to understand the rock-fluid interactions, we wanted to study how simpler brines induce chemical and mechanical alterations to the rock properties. Such as it is, we go on to study the role of Mg^{2+} in more detail.

2. Methods

2.1. The Chalk

The experiment was performed on outcrop chalk collected from Liège in Belgium. Chalk is a sedimentary rock with high calcium carbonate ($CaCO_3$) content. The concentration of $CaCO_3$ for Liegè chalk was measured by *Zimmermann et al.* [2015], *Hjuler and Fabricius* [2009], and *Megawati et al.* [2012] and the reported values range from 91% to 95%. A cylindrical plug was drilled from a chalk block before being radially adjusted to the desired initial diameter D_0. Then, the cylinder was cut (trimmed) to the desired length L_0. Each end piece was stored to ensure that the tested and untested material could be compared using analytic tools. Before testing, the plug was put in a drying cabinet at 100°C overnight before the initial dry mass was measured ($M_{s,0}$). The plug was then placed in a vacuum cabinet before being saturated by distilled water for saturated weight measurements ($M_{\mathrm{sat},0}$). The weight difference between the saturated and dry mass is used to estimate the pore volume, and hence the porosity before testing ϕ_0. The initial length, diameter, and saturated and dry mass are presented in Table 1. The porosity estimate from the pycnometer measurement of the solid density is 0.4% higher than the porosity estimate from the weight difference between the dry and saturated mass, indicating ~99% saturation.

After the experiment, the solid volume of core material samples was measured with a helium gas pycnometer (Micromeritics Gas Pycnometer model AccuPyc II 1340). The average mineral density is estimated from the dry mass divided by the solid volume. Density is measured on both unflooded (Table 1) and flooded chalk materials (Table 5).

Table 1. Initial Values for the Liège Chalk Core Used in the Experiment (ID: L18)

Parameter	Value
Dry weight, $M_{dry,0}$ (same as solid weight M_s)	125.57 g
Wet weight, $M_{sat,0}$	158.56 g
Initial pore volume, $V_{p,0}$	32.99 cm^3
Length, L_0	7.008 cm
Diameter, D_0	3.810 cm
Bulk volume, $V_{b,0}$	79.84 cm^3
Porosity, φ_0	41.32% (equation (13))
Solid density, $\rho_{s,0}$ (from saturated and dry weight)	2.68 g/cm^3
Solid density, $\rho_{s,0}$ (from pycnometer)	2.70 g/cm^3
Porosity, φ_0	41.74% (equation (14))
Solid volume, $V_{s,0}$	46.85 cm^3

2.2. The Triaxial Cell and Experimental Setup

The chalk plug was mounted into a triaxial cell that allows for continuous measurements of the axial and radial strains during flooding reactive fluids at elevated stresses, pressures, and temperatures (see Figure 1). The cell was equipped with a heating jacket and regulating system (Omron E5CN) with precise temperature control (±0.1°C). The temperature was set to 130°C and monitored by a Pt-100RDT resistance temperature detector inside the cell. Three pumps were connected to the cell allowing for independent control of the piston pressure (P_{pist}), radial confining stress (σ_{rad}), and injection flow rate (q_{in}) (Gilson Pump Model 307 HPLC). The pore pressure was controlled by a backpressure regulator ensuring constant pore pressure at 0.7 MPa on the outlet side of the core (downstream). The backpressure regulator allowed for continuous sampling of the effluent water throughout the test period. The axial stress was calculated from the confining pressure (i.e., radial stress), piston pressure, frictional pressure of the piston movement in the triaxial cell (P_{fric} = 0.4 MPa), and an area factor for the piston pressure chamber and the cross area of the plug (f_{area} = 1.27):

$$\sigma_{ax} = \sigma_{rad} + f_{area}\left(P_{pist} - P_{fric}\right) \quad (1)$$

The position of the piston, and hence the length of the plug (L), was monitored by an external linear voltage differential transducer placed on top of the piston. The radial strain was measured with an extensometer that measures the circumferential diameter on the middle of the core (failed at 113 days).

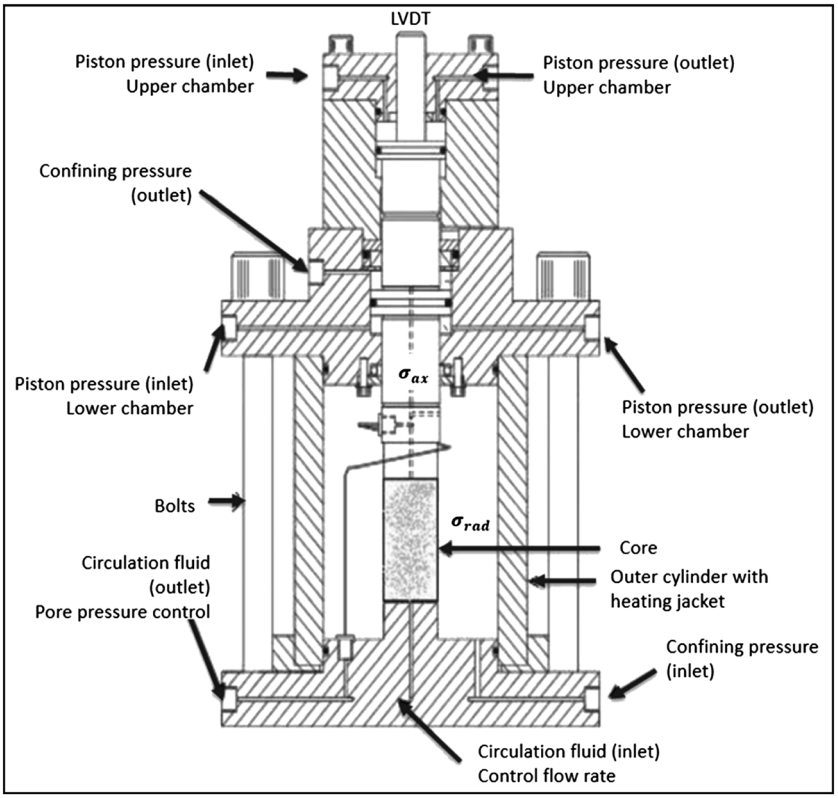

Figure 1. Sketch of the experimental setup.

Table 2. Chemical Composition of the Fluid Used in the Experiment[a]

Injection Fluid	Molar Strength (*M*)	Weight Per Liter Solution (g/L)	Flow Sequence During Creep Time (days)
NaCl	0.657	38.40	1–7
$MgCl_2$	0.219	20.84	7–56
Distilled water	—	—	56–67
$MgCl_2$	0.219	20.84	68–1072

[a]Injection volume flux (q_{in}) varied between 33.12 and 99.36 cm^3/d.

The injected pore fluid was mixed according to the desired chemistry (see Table 2) and flooded through the plug at varying injection volume fluxes (q_{in}) (see Table 3). The injected flow set up a hydraulic pressure difference across the plug (dP) that was stored and used to estimate the permeability (assuming Darcy's law for laminar flow in porous media):

$$k = \frac{4\mu_w L q_{in}}{\pi D^2 \Delta P} \tag{2}$$

where the cross-sectional area is given by $\pi D^2/4$, plug length is L, and viscosity of μ. The pressure difference, stress state, and strain dynamics were logged in LabView to study how the plug responded to the injected fluid during testing.

The experiment was performed according to the following stages:

1. Loaded to 1.2 MPa confining pressure and 0.7 MPa pore pressure during washing with distilled water (DW) with three initial pore volumes, from now on abbreviated as PVs. During this period, the initial permeability was measured.
2. Saturated the core with NaCl brine.
3. Raised the temperature from ambient to 130°C.
4. Increased the confining pressure at hydrostatic conditions, where the piston pressure is kept 0.1 MPa above the friction of the piston (~0.4 MPa). From hereon, the stress condition is referred to as hydrostatic. The confining pressure σ was increased from 1.2 to 11.1 MPa over a time interval of 380 min. During this phase, the elastic and plastic parameters were measured from stress-strain plots. The initial phases from (1) to (4) lasted 3 days.
5. Creep at constant hydrostatic stress conditions for 1072 days while flooding brines at desired chemistry according to Table 2. Pore pressure and confining pressure were kept constant throughout the test at 0.7 and 11.1 MPa, respectively.
6. The flow rate was changed between one and three PVs per day based on original pore volume (i.e., 33.12 and 99.36 cm^3/d) four times throughout the test (see Table 3). A total of 72.0 L of $MgCl_2$ brine was flooded through the core during the 1072 days.

2.3. Ion Chromatography

Effluent samples were collected approximately three times a week during the test period and more frequently in the time period when flooding fluids were changed. The effluent samples were diluted 500 times with distilled water on a Gilson GX-271 machine. The dilution was done to meet the linear region of the calibration curve of the Dionex ICS-3000 ion chromatograph. In the chromatograph, the concentration of four anions (IonPac AS16 exchange column) and three cations (IonPac CS12A exchange column) can be estimated from the areas under the chromatographic curves when compared to known standards. Here we report the Mg^{2+} and Ca^{2+} concentrations at any time. The pH was measured in the effluent water. The pH is heavily affected by the CO_2 concentration. The saturation of CO_2 in water depends on temperature and pressure, as CO_2 boils off when water is cooled down and transported through the backpressure regulator. In this paper, we report the uncorrected measurements that were taken several months after the

Table 3. Flow Rates Used in the Experiment

Creep Time (Brine Used)	Flow Rate
0–112 days (NaCl, DW, and $MgCl_2$)	33.12 cm^3/d
112–368 days ($MgCl_2$)	99.36 cm^3/d
368–777 days ($MgCl_2$)	33.12 cm^3/d
777–1072 days ($MgCl_2$)	99.36 cm^3/d

samples were acquired. Therefore, the reported pH measurements do not match the pH of the water that exits the cores; however, the reported measurements are important to understand the dynamic evolution and trends in the experiment.

3. Theory

3.1. Constitutive Relations for the Volume Evolution of Biphase Materials

This section focuses on the formalism needed to analyze together the measurements that were performed before test, during test, and after test. The bulk volume (V_b) of a biphase material equals the sum of the solid volume (V_s) and the pore volume (V_p.):

$$V_b = V_p + V_s \tag{3}$$

Any changes to the total volume are given by changes in pore volume and solid volume:

$$\Delta V_b = \Delta V_p + \Delta V_s. \tag{4}$$

In this analysis, we keep track of the bulk volume from the volumetric strain and use the ion concentration of the produced fluids to estimate the solid volume. Before testing, the plug was drilled in a cylindrical shape such that the initial bulk volume was simply given by the cylinder volume. After testing, the plug is nonhomogenously deformed such that the bulk volume is given by the sum of truncated wedges:

$$V_b = \sum_i \frac{\pi h_i}{12}\left(D_i^2 + D_{i+1}^2 + D_i D_{i+1}\right) \tag{5}$$

where we measure the diameter $(D_i)t$ intervals along the plug h_i and sum over all contributions.

3.2. Strain Measurements

Axial (ε_{ax}), radial (ε_{rad}), and volumetric (ε_{vol}) strains are estimated from the length and diameter measurements according to

$$\varepsilon_{ax} = -\frac{L - L_0}{L_0} \tag{6}$$

where L is the length of the core during the experiment and L_0 is the original length. The volumetric and radial strain is defined in a similar way:

$$\varepsilon_{rad} = -\frac{D - D_0}{D_0} \quad \text{and} \quad \varepsilon_{vol} = -\frac{V_b - V_{b,0}}{V_{b,0}} \tag{7}$$

If the core keeps a cylindrical geometry, the volumetric strain can be calculated from the axial and radial strain from the equations above:

$$\varepsilon_{vol} = \varepsilon_{ax} + 2\varepsilon_{rad} + 2\varepsilon_{ax}\varepsilon_{rad} + \varepsilon_{rad}^2 + \varepsilon_{ax}\varepsilon_{rad}^2 \tag{8}$$

Because of failure of the radial strain gauge, we only have insight into the radial strain measurements from the first 113 creep days. Nevertheless, a simplified assumption can be made to convert the axial strain measurements to the volumetric strains, by introducing a conversion factor ξ such that $\varepsilon_{rad} = \xi\varepsilon_{ax}$. It is assumed that ξ remains constant throughout the test; hence,

$$\varepsilon_{vol} = (1 + 2\xi)\varepsilon_{ax} + \left(2\xi + \xi^2\right)\varepsilon_{ax}^2 + \xi^2\varepsilon_{ax}^2 \tag{9}$$

The conversion factor is estimated by demanding that the volumetric strain matches the measured volume of the core after the experiment (Table 5).

3.3. Stress-Strain Relations

During loading (stage 4; section 2.2 above), the hydrostatic stress (confining pressure) is increased to 11.1 MPa over 380 min. Stress-strain relations are shown where the effective stress of a porous material is

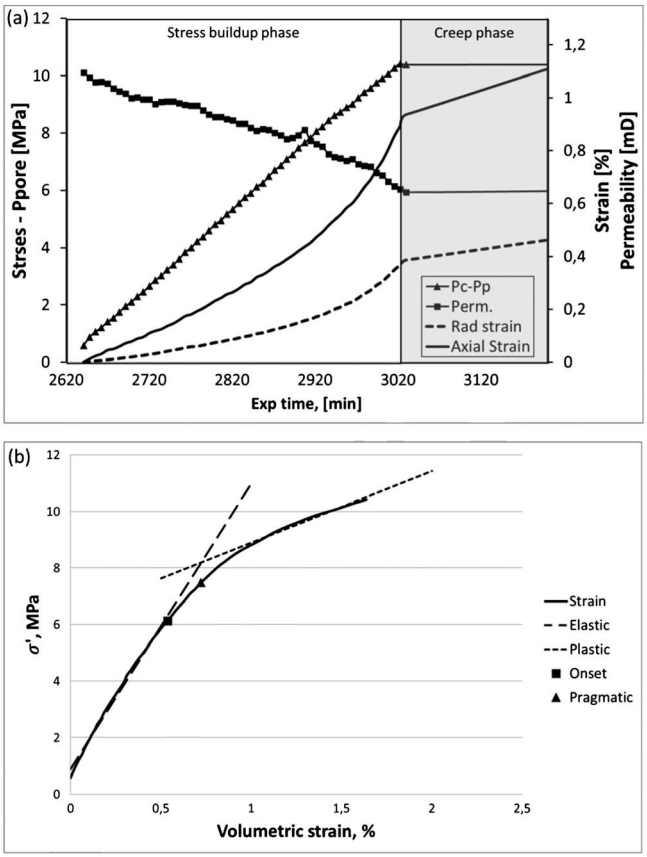

Figure 2. (a) The external stress (triangles), the permeability (squares), radial strain (stippled line), and axial strain (solid line) plotted over time during continuous flow of NaCl brine at 33.12 mL/d and 130°C. (b) Stress and volumetric strain during loading. Lines fitted to the linear elastic and plastic phase. Yield points are shown.

calculated from the Biot effective stress relation [*Biot*, 1941; *Charlez*, 1991] where the total imposed stress (σ) is reduced by a fraction α of the internal pore pressure (P):

$$\sigma' = \sigma - \alpha P \tag{10}$$

where α is termed the Biot coefficient. For low pore pressures, as is the case here, the exact value of the Biot coefficient is not that important, and we equal this to 1. In drained hydrostatic experiments, the volumetric strain is linked to the effective stress via the drained bulk compressibility of the rock framework K_{fr} [*Fjær et al.*, 2008]:

$$\sigma' = K_{fr}\varepsilon_{vol} \tag{11}$$

Beyond a certain stress level during stress buildup, the observed strain dynamics deviate from the initial linear response. The onset of nonlinearity is a signature of irreversible deformation associated with grain reorganization and pore collapse (note that irreversible deformation could also occur at low stresses due to, e.g., the closure of microcracks that may form during the rock sampling and preparation of the cores). When the deviation exceeds a set threshold of 0.2 MPa, the onset of yield (Y_{vol}) is defined. A new linear stress-strain relation is observed when the hydrostatic stress is increased farther into the plastic regime. This slope is termed the plastic modulus $K_{fr,vol}$, also using equation (11).

As is often the case for chalks, yielding occurs over a range of stresses between the onset of yield in the lower end and the onset of linear plastic behavior in the upper. The range of stresses may be approximated by the pragmatic yield ($Y_{p,vol}$). The pragmatic yield (also termed typical yield) is defined to occur at the stress corresponding to the strain at which the elastic and plastic curves intercept (Figure 2). The bulk modulus in the elastic and plastic regime, together with the onset and pragmatic yields, are reported in Table 4.

3.4. Porosity Estimates Before and After the Test

At any given time during the test, the porosity is given by the proportion of pore volume to the total volume:

$$\phi = \frac{V_p}{V_b} = 1 - \frac{V_s}{V_b}, \tag{12}$$

Table 4. Stress Buildup Rate of 0.025 MPa/min[a]

	Elastic Bulk Modulus, K_{fr} (MPa)	Plastic Bulk Modulus (Plastic), $K_{fr,pl}$ (MPa)	Onset of Yield, Y_{ons} (MPa)	Pragmatic Yield Y_{pragm} (MPa)
Volume	1011 ± 15	253 ± 10	6.1	7.5
R^2	0.99	0.98		

[a]Elastic parameters obtained from the effective stress interval from 0.5 to 4.6 MPa and plastic parameters from 8.7 to 10.4 MPa. R^2 is given to the linear fit.

Table 5. Measurements of the Plug After Test

Chalk ID: L18, Liège, 130°C		Measurement Used
Test days	1072 days	
Saturated weight	126.34 g	
Dry weight	102.64 g	Measured mass loss of 22.70 g on scale
Pore volume	23.71 cm^3	From the difference in saturated and dry weight
Length	6.247 cm	
Axial strain	10.80%	From the length before test, equation (6)
Average diameter	3.491 cm	See Table 6
Total volume after test	59.23 cm^3	Calculated by truncated wedge, equation (5); see Table 6
Volumetric strain	25.81%	From the measured volume before and after test, equation (7)
Axial to volume factor, ξ	0.59	Volume strain estimated from axial strain, equation (9)
Porosity	40.02%	From the pore volume divided by volume after test, equation (13)
Average solid density	2.89–2.90 g/cm^3	Pycnometer measurement, average of all pieces
Solid volume	35.21 cm^3	Dry weight divided by solid density
Solid volume	35.53 cm^3	Total volume minus the pore volume
Porosity	40.14%	From the dry mass, volume and pycnometer density, equation (14)

where equation (3) is used in the second term. In the experiment, porosity was measured in two ways, both before and after the test. In the first method, the porosity was estimated from the weight difference between the dry (i.e., weight of the solids M_s) and distilled water saturated plug (i.e., weight of the solids plus the water in the pores M_{sat}), divided by the density of the distilled water (ρ_{dw}) and the measured bulk volume:

$$\phi = \frac{M_{sat} - M_s}{\rho_{dw} V_b}. \tag{13}$$

The second way of measuring the porosity is by pycnometer measurements of the solid volume, which can also be used to estimate the average mineral density:

$$\phi = 1 - \frac{V_s}{V_b} = 1 - \frac{M_s}{\rho_s V_b} \tag{14}$$

The values from equations (13) and (14) are shown before and after the test in Tables 1 and 5.

3.5. Estimating the Change in Solid Volume

The evolution of the solid mass over time within the plug is given by the difference in chemical flux into the core and out of the core. The chemical flux is constrained by monitoring the effluent concentration of different ions over time. Over a time interval δt, the difference in mass is given by

$$\frac{\delta M_s}{\delta t} = \sum_j \left(c_{in,j} - c_{out,j}\right) q M_{wj} \tag{15}$$

where $c_{in,j} - c_{out,j}$ is the difference in the ion composition (mol/L), q is the flow rate (L/d), and M_{wj} is the molar weight (g/mol) of species j (magnesium and calcium ion). The molar weights of calcium and magnesium are 40.08 g/mol and 24.31 g/mol, respectively. In the presented analysis, we omit any production of the carbonate ion (CO_3^{2-}) in the effluent brine and thereby make the simplifying assumption that all the initial carbonate ions are bound to the calcium and that the retained magnesium binds to form dolomite (Mg,Ca) CO_3 or magnesite $MgCO_3$. We are forced to make this assumption, as the evolution of CO_3 content over time was not measured. The accumulated mass change at any given time (t) throughout the test period is estimated from the integrated sum of all sample analyses:

$$\Delta M_s(t) = \int_0^t \frac{\delta M_s}{\delta t'} \mathrm{d}t' \tag{16}$$

where the integrand is taken from equation (11). Given the knowledge on the density evolution of the solid constituent, we can now estimate the volume of solids through

$$\Delta V_s(t) = \frac{M_s(t)}{\rho_s(t)} - \frac{M_{s,0}}{\rho_{s,0}} \tag{17}$$

In equation (17), the mass evolution and the density before experiment are known quantities, while the density evolution is unknown. To overcome this, we use a density evolution function which depends on the normalized amount of calcium left in the plug $\widetilde{m}_{Ca}(t)$ and the initial and final densities:

$$\rho_s(t) = \widetilde{m}_{Ca}(t)\rho_{s,0} + (1 - \widetilde{m}_{Ca}(t))\rho_{s,f} \tag{18}$$

where the normalized amount of calcium in the plug runs from 1 to 0 and is calculated via

$$\widetilde{m}_{Ca}(t) = \frac{M_{Ca}(t) - M_{Ca,final}}{M_{Ca,init} - M_{Ca,final}} \tag{19}$$

where $M_{Ca}(t)$ is the calcium mass at time t. Now the strategy is to use the initial calcium weight minus the produced calcium (using equation (16)) into equations (18) and (19) to estimate the average density at any given time.

Alternatively, the solid volume can be estimated from the mineral constituent in the core:

$$V_s(t) = V_{s0} + \Delta V_s = V_{s0} + \Delta V_{magn} + \Delta V_{calc} + \ldots \Delta V_i \tag{20}$$

Under the assumption that the constituency of all minerals i can be estimated from the produced ion concentration, we can use the molar volume $\widetilde{V_i}$ and the change in number of moles Δn_i for all minerals i:

$$V_s(t) = V_{s0} + \sum_i \Delta n_i \widetilde{V}_i \tag{21}$$

3.6. Dynamic Porosity Estimates

At any given time, the porosity may be expressed through the initial pore volume ($V_{p,0}$) and bulk volume ($V_{t,0}$) plus the changes in both variables:

$$\phi(t) = \frac{V_{p,0} + \Delta V_p}{V_{b,0} + \Delta V_b} \tag{22}$$

In these tests' designs, the evolution in pore volume was unknown. As such, for biphase materials, we may use equation (4) to estimate the pore volume changes from changes in the bulk volume minus changes in the solid volume:

$$\phi(t) = \frac{V_{p,0} + \Delta V_b - \Delta V_s}{V_{b,0} + \Delta V_b} \tag{23}$$

If we divide by $V_{b,0}$ and introduce the initial porosity $\phi_0 = V_{p,0}/V_{b,0}$ and the volumetric strain $\varepsilon_{vol} = \Delta V_b/V_{b,0}$, we get an expression of the average plug porosity over time:

$$\phi(t) = \frac{\phi_0 + \varepsilon_{vol} - \Delta V_s/V_{b,0}}{1 + \varepsilon_{vol}} \tag{24}$$

where the volumetric strain is estimated from the axial strain measurements from equation (9) and the solid volume evolution from equation (17). In the following, it is assumed that the volumetric strain and solid volume evolution are homogenously distributed throughout the sample. However, as equation (24) is derived, it is, in principle, capable of incorporating nonhomogenous development of the porosity, when spatial strain field and dissolution/precipitation dynamics are known.

Within this analysis, the porosity may be estimated at any time with the volumetric strain in equation (9), and solid volume changes (equation (17)) are known:

$$\phi(t) = \frac{\phi_0 + \varepsilon_{vol}(t) - \frac{1}{V_{b,0}}\left(\frac{M_s(t)}{\rho_s(t)} - \frac{M_{s,0}}{\rho_{s,0}}\right)}{1 + \varepsilon_{vol}(t)} \tag{25}$$

In the discussion section, we will address the measured hydraulic permeability development (equation (2)) in light of the estimated porosity development.

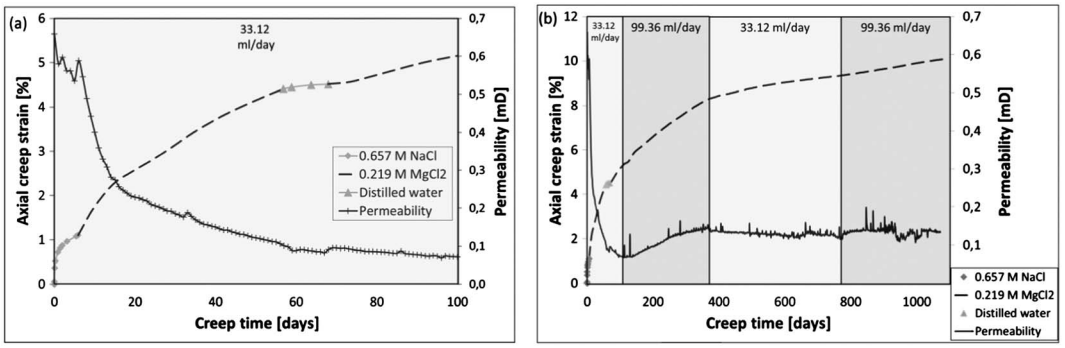

Figure 3. Axial creep and permeability over time periods of (a) the first hundred days and (b) the whole creep period. Flow rates are shown in the figure. Note how the brine composition affects strain rate at 7, 56, and 67 days and how the permeability develops over time.

4. Results

In this section, results are divided into five parts in which stress-strain curves during loading are shown in section 4.1, strain and permeability measurements during creep are shown in section 4.2, while results of effluent water analyses are presented in section 4.3. Core analyses before and after the test are presented in section 4.4, and the structural difference between tested and untested materials analyzed using scanning electron microscopy (SEM) and energy dispersive spectroscopy (EDS) is reported in section 4.5.

4.1. The Stress Buildup Phase: Work Diagram

The loading phase was performed at 130°C with continuous flooding of NaCl at 33.1 cm^3/d flow rate. As shown in Figure 2a, the imposed effective stress was increased from 0.5 to 10.4 MPa (i.e., 11.1–0.7 MPa) over 380 min (triangles), giving a stress buildup rate of 0.025 MPa/min. The corresponding permeability evolution (in millidarcy) was plotted with squares, and the axial and radial strains (in percent) are plotted using solid and dashed lines, respectively. The sedimentary bedding direction compared to the axial direction was investigated by, e.g., *Korsnes et al.* [2008b] on Liège outcrop cores, and anisotropic behavior was observed. However, an overall observation from many other experiments on chalk shows that less strain is accumulated in the radial compared to the axial direction, due to the geometry of the experiment. In Figure 2b, the work diagram plotted imposed stresses along the left *y* axis and the observed volumetric strain along the *x* axis. At low stresses (quasi-elastic regime) and high stresses (plastic regime), we obtained a more or less linear relationship between the imposed stresses and the observed strains. Linear curves were fitted to these regions (black dashed and dotted lines), which were used to obtain the onset of yield and pragmatic (typical) yield stresses. All values are listed in Table 4.

4.2. The Creep Phase

The deformation at constant stress and pore pressure condition, termed creep, lasted for 1072 days with continuous logging of the axial strain and hydraulic permeability during flow of various brines (Table 2) and rates (Table 3). Figure 3a displays how the brine composition affects the observed axial creep strain over the first 100 days. At the same time, the logarithm of the strain rate is shown against time in Figure 4a and against total creep in Figure 4b. Initially, the core was flooded with NaCl brine during the loading phase and the first 7 days of creep (Figure 3a, diamonds), before $MgCl_2$ flow started (stippled line). The flow of $MgCl_2$ brine led to an abrupt increase in the axial strain rate. At 57 days, the injection of distilled water (DW) led to an abrupt reduction in the observed strain rate. At 68 creep days, the $MgCl_2$ flooding was restarted, again leading to increased creep rate.

From 68 days until the end of the experiment, the brine composition was kept constant ($MgCl_2$), and the effect of flow rate was studied. The flow rate was changed three times during the experiment, namely, at 112, 368, and 778 days (e.g., shown in Figures 3 and 4). Figure 3b shows how the observed creep depends on the flow rate. Overall, the observed strain rate reduced over time, although the strain at any given time positively correlated to the flow rate. For example, at 112 and 778 days, the flow rate was increased to 99.36 cm^3/d, leading to an increase in the strain rate (Figure 4b). Vice versa, at 368 days, the flow rate was

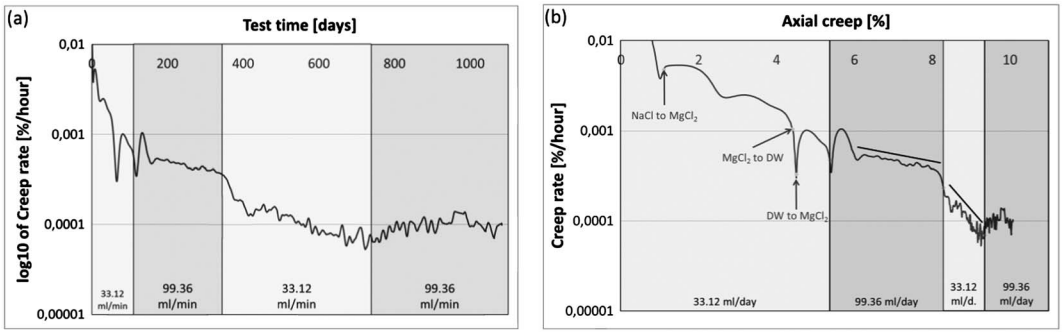

Figure 4. (a) Log linear plot of axial strain rate over time shows how the strain rate is affected by the flow rate. At 368 days, strain rate is reduced by a factor of 3 from ~3e−4%/h to ~1e−4%/h when the flow rate is reduced by a factor of 3 from 99.36 cm^3/d to 33.12 cm^3/d. At 778 days, the strain rate increased when the flow rate was increased trebled. (b) Logarithmic creep rate versus axial creep strain. Note how changing from $MgCl_2$ to DW reduced the strain rate and how the strain rate increased again when $MgCl_2$ was reinjected. Note also how the strain rate was sensitive to flow rate. Black lines are introduced to guide the eye.

reduced to 33.12 cm^3/d, leading to a reduced strain rate showing how the pore fluid composition alters the dynamic strength of Liegè chalk.

Note that although the strain is increasing during the whole experiment, the permeability is reduced on the first ~115 days, before it starts increasing until a stable plateau is reached after ~400 days.

4.3. Ion Chromatography Analysis

The nonequilibrium of the rock-fluid interface changes the ion concentration of the effluent brine. The effluent was sampled three times per week during the whole creep phase (except from 800 to 900 days). For each sample, the ion concentration of two cations (magnesium and calcium) and one anion (chloride) is reported. The time evolution of the ion concentration for the three ions is plotted in Figure 5a. In

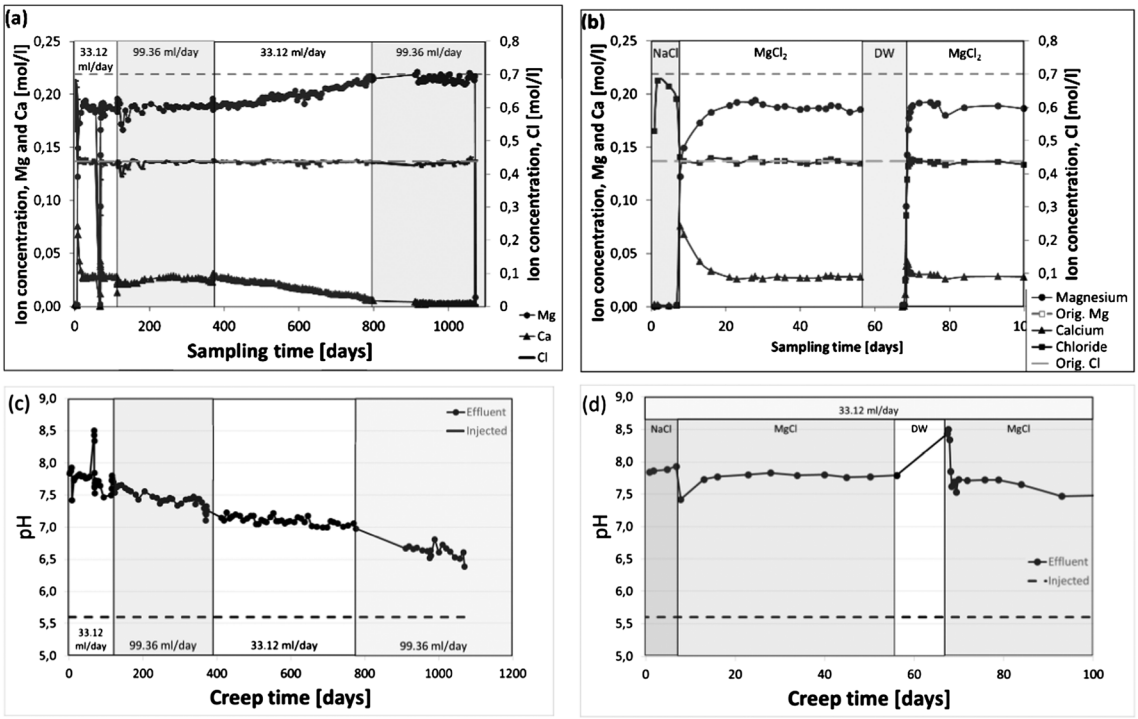

Figure 5. (a and b) The effluent ion concentration of calcium, magnesium and chloride over time (whole test and first 100 days). Magnesium is lost to the core (green squares) compared to the dashed green line of the inlet concentration in mol/L. Calcium is produced (red triangles) from the plug. (c and d) The evolution in pH in the effluent sample compared to the injected pH. Note that the pH increased at a constant reducing degree.

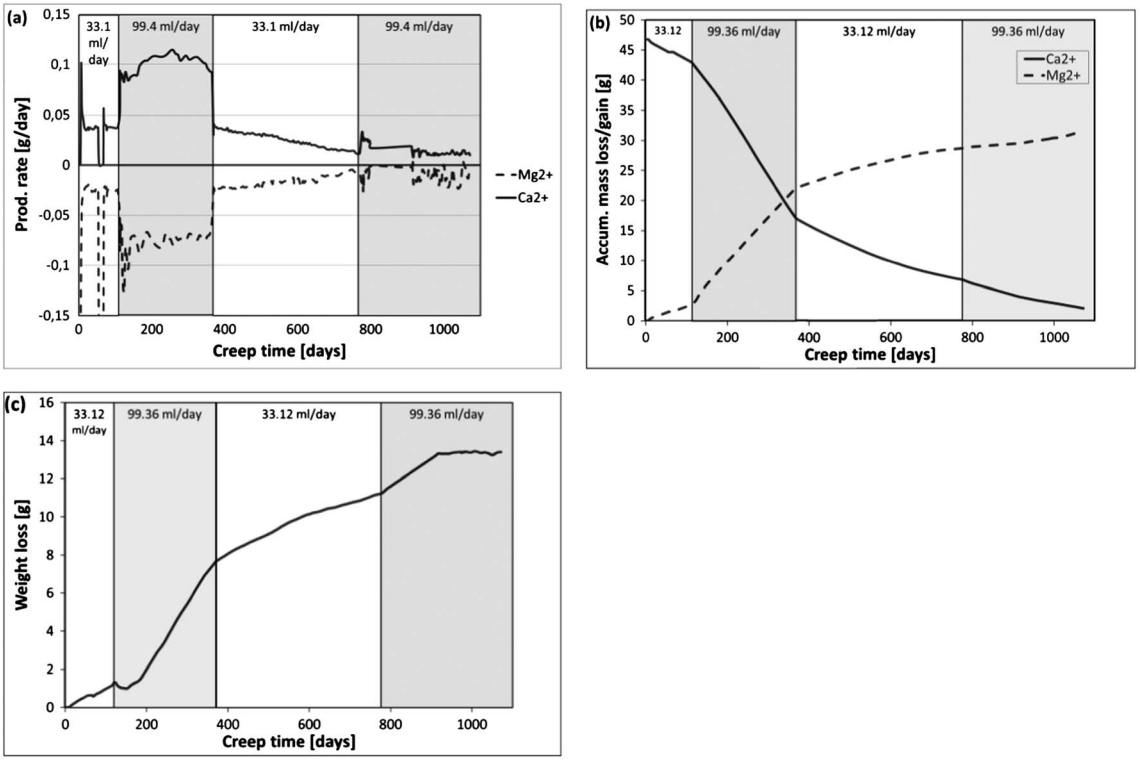

Figure 6. (a) Evolution in the production rate of Mg^{2+} and Ca^{2+} over time. (b) Integrating the rate of change enabled the calculation of the amount of Mg^{2+} and Ca^{2+} in the core. (c) Total weight loss from the difference between the Ca^{2+} evolution and Mg^{2+} evolution in Figure 6b.

Figure 5b, we zoom into the first hundred days of the experiment. The effluent concentration of chlorine is very close to the inlet concentration. It can be viewed as a nonreactive tracer. Calcium is produced and magnesium ions are retained within the plug. When changing from NaCl to $MgCl_2$ at 7 days, we can see a transient behavior in the calcium production and magnesium retention, until a stable production/loss is reached at ~20 days. Samples were not collected during the DW flooding from 56 to 67 days. When $MgCl_2$ flooding was restarted at 67 days, we did not observe the same transient behavior as when the $MgCl_2$ flooding was started from the NaCl flooding at 7 days. Figure 5a shows the evolution in the ion concentration for the whole experiment time until 1072 days. Several interesting observations can be made: (1) the calcium concentration is sensitive to changes in the flow rate, as an increased flow rate reduces the concentration at 112 days, and vice versa at 368 days. This indicates that the fluid retention time within the core is inadequate for the fluid to equilibrate with the chalk. Such a flow rate dependency in the produced Mg concentration is, however, not so clear at 368 nor at 112 days. From ~400 days, the produced calcium was reduced over time and fell near 0 after 900 days.

Table 6. Diameter Measurements From Inlet (Left) to the Outlet (Right)[a]

Length From Inlet (cm)	Diameter (cm)
0	3.550
0.5	3.423
1	3.409
2	3.430
3	3.460
4	3.476
5	3.489
5.5	3.432
6.247	3.548
Total volume	59.23 cm^3

[a]Calculated bulk volume from truncated wedge (equation (5)).

Even though the calcium concentration decreased when the flow rate was increased (Figure 5a), there was a larger dissolution in gram per day (Figure 6). The dissolution rate of calcium increased almost by a factor of 3 from ~0.04 to 0.10 g/d at 112 days. From 367 days, the dissolution rate was lowered by approximately the same amount. From 400 to 800 days, the rate of calcium dissolution declined as the amount of calcium left in the core was reduced over time (Figure 6b, solid line). The

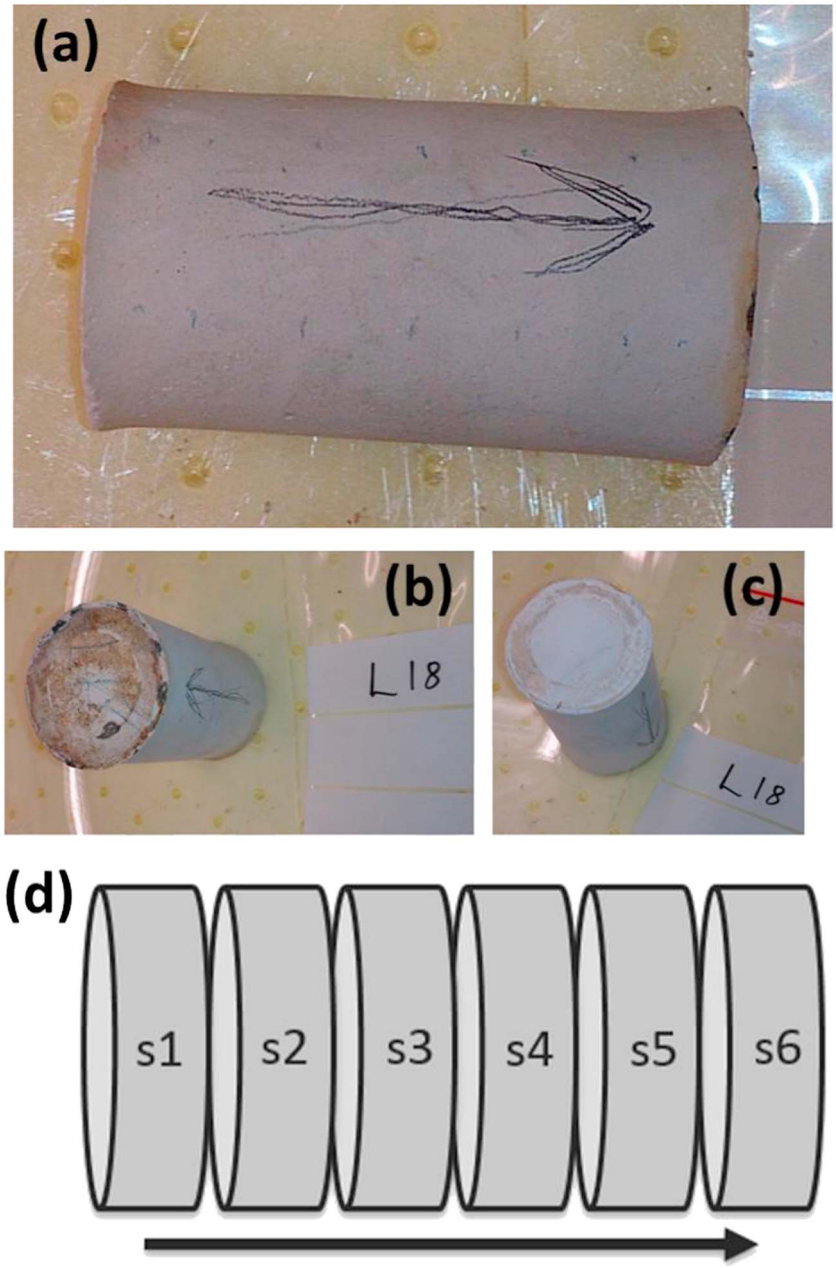

Figure 7. Pictures of the plug after the test. (a) Side view, (b) outlet side, and (c) inlet side. After the experiment, the core was cut into six slices, enumerated from inlet to outlet.

reduced amount of calcium that remained in the plug could have reduced the reactive surface area, thereby reducing the overall production rate. The integrated total produced calcium from the plug was 1.12 mol (44.7 g).

The rate of magnesium retained within the core follows the same trend as the Ca produced from the plug, more or less. This implies that stoichiometric effects are important in these systems. However, there are some clear deviations between Mg-Ca stoichiometry and what was measured: (a) the Mg concentration fluctuated more than the Ca concentration (in absolute terms), but the relative variability (divided by the average value) for Mg and Ca is comparable. (b) The same flow rate dependency in the measured Mg loss, as is observed for the Ca concentration, is not observed. This is clearly seen in Figure 5a, at 112 days, where the Ca concentration of the produced effluent reduced, as the injection rate increased by

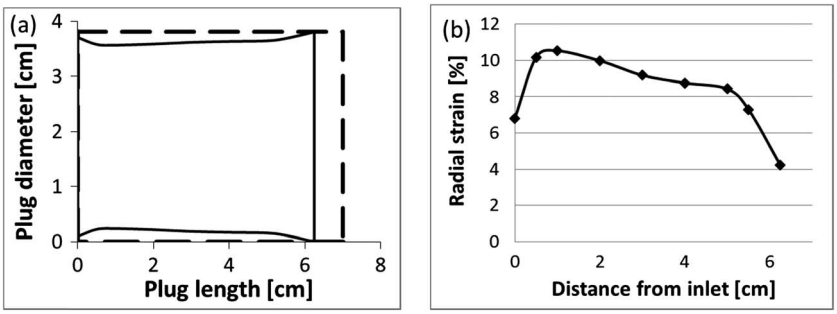

Figure 8. (a) Plot of the external geometry of the plug after the test. Inlet side is to the left and the outlet side to the right. (b) The radial strain from the inlet toward the outlet.

a factor of 3. At 378 days, when the flow rate was reduced, the effluent Ca concentration increased. This is not observed for the Mg ion. (c) The total amount of Mg retained within the core added up to 1.28 mol (31.2 g) while 1.12 mol Ca was produced. In all, a–c indicated that more complex geochemical processes occurred, besides the ion exchange.

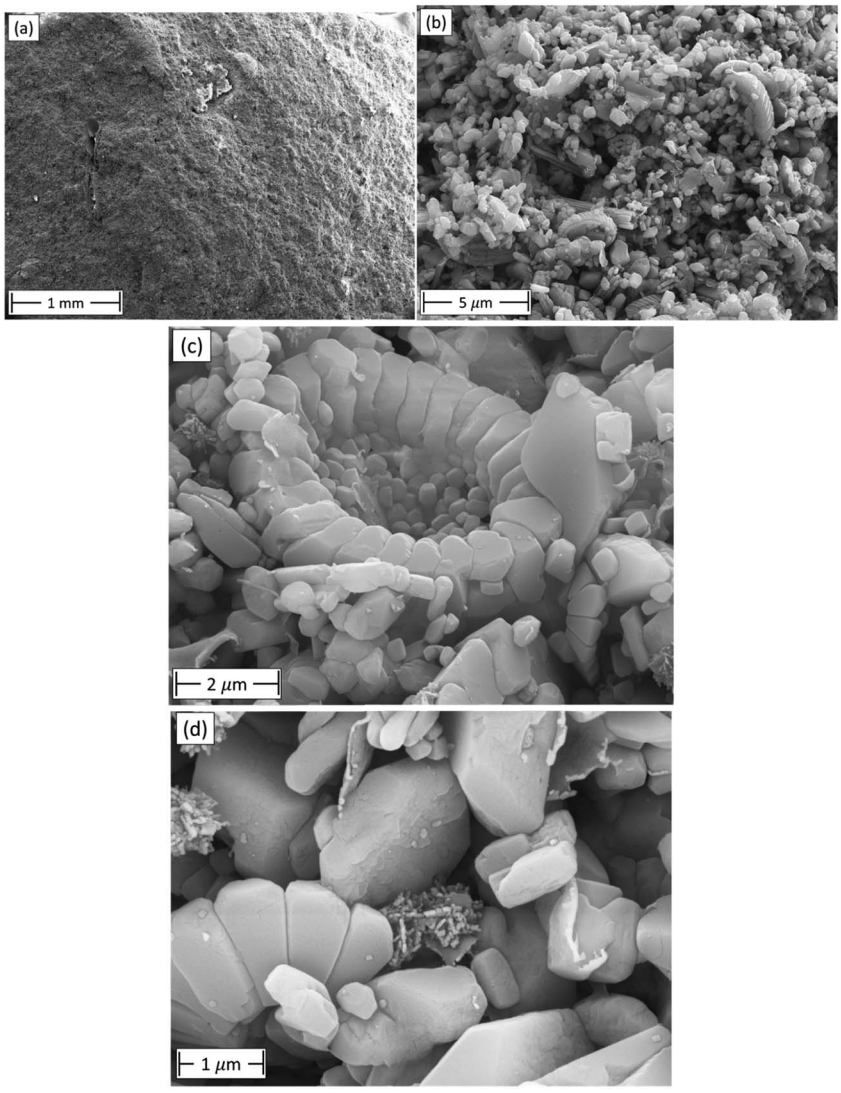

Figure 9. SEM image of untested Liège chalk material from the end slices on each side of the core (trimming). Scale bare is shown in each image.

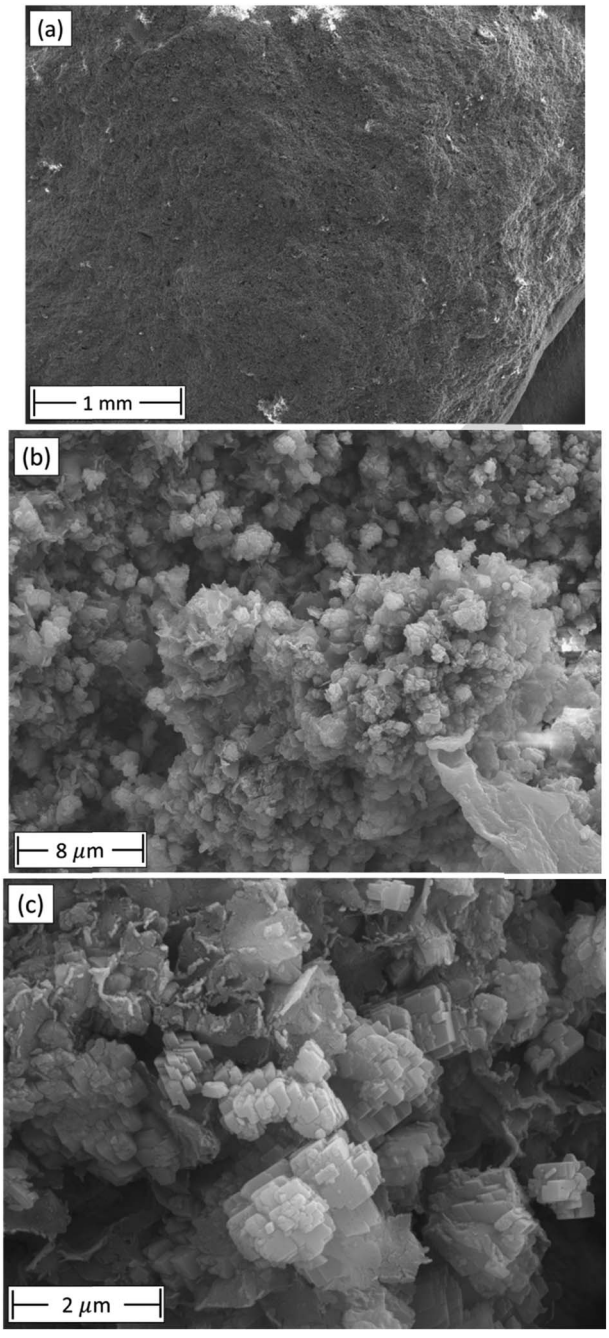

Figure 10. SEM image of tested core material from slice 2. The width of each image is 3580, 37, and 8 μm. Complete reworking of the microstructure can be seen compared to SEM images in Figure 9.

Figure 6a shows the total amount of calcium and magnesium in the core with time estimated from the initial values, 1.17 mol and 0 mol, respectively (Table 7). From 112 to 367 days, the amount of calcium was reduced to 17 g, while the magnesium was increased to 22 g, respectively. After 367 days, the rate of Ca production and Mg loss was reduced. From 778 to 1072 days, the remaining calcium is reduced to 4.36 g and the total weight of all retained magnesium ions is 31.52 g. The difference between the magnesium gain and calcium loss is plotted in Figure 6b, adding up to 13.42 g at the end of the experiment.

4.4. Analyzing the Core After Test

Measurements of the core before and after the test are shown in Tables 5 and 6. Before demounting the plug, it was saturated by DW and its saturated weight was measured. The plug was placed in a heating cabinet overnight to measure the dry weight. The difference between the saturated and dry weight yields an estimate of the pore volume. Through the experiment, pore volume was reduced from 32.99 cm^3 to 23.71 cm^3. The bulk volume was estimated from the length and diameter measurements displayed in Table 6, where diameters were measured along the core to calculate the bulk volume (equation (5)). The porosity and solid volume were estimated from the pore and bulk volume after the test, to be 40.02% (equation (13)) and 35.53 cm^3, respectively. The total volume strain was estimated to 25.81%. In order to estimate the time evolution of the volumetric strain at any given time, the axial strains were converted to the volumetric strain using equation (9) with the factor $\xi = 0.59$ that fits the external volume after the test. The core was cut into six pieces and the solid density was measured using the helium gas pycnometer on all pieces. The density variation held a more or less constant value of 2.89–2.90 g/cm^3 along the core, indicating a complete and homogeneous chemical reworking. Based on the solid density, dry mass, and bulk volume, we estimated the porosity and solid volume to be 40.14% and 35.21 cm^3 (using equation (14); see Table 5). These measurements of porosity and solid volume are very close to the estimates obtained from the measurement of the saturated-dry weight difference performed directly on the scale (35.53 cm^3 and 40.02%; Table 5). The side view of the chalk plug after the experiment can be seen in Figure 7a, while Figures 7b and 7c show the outlet and inlet sides, respectively, while the external geometry of the plug before and after test is displayed in Figure 8. As can be seen, the degree of radial compaction along the

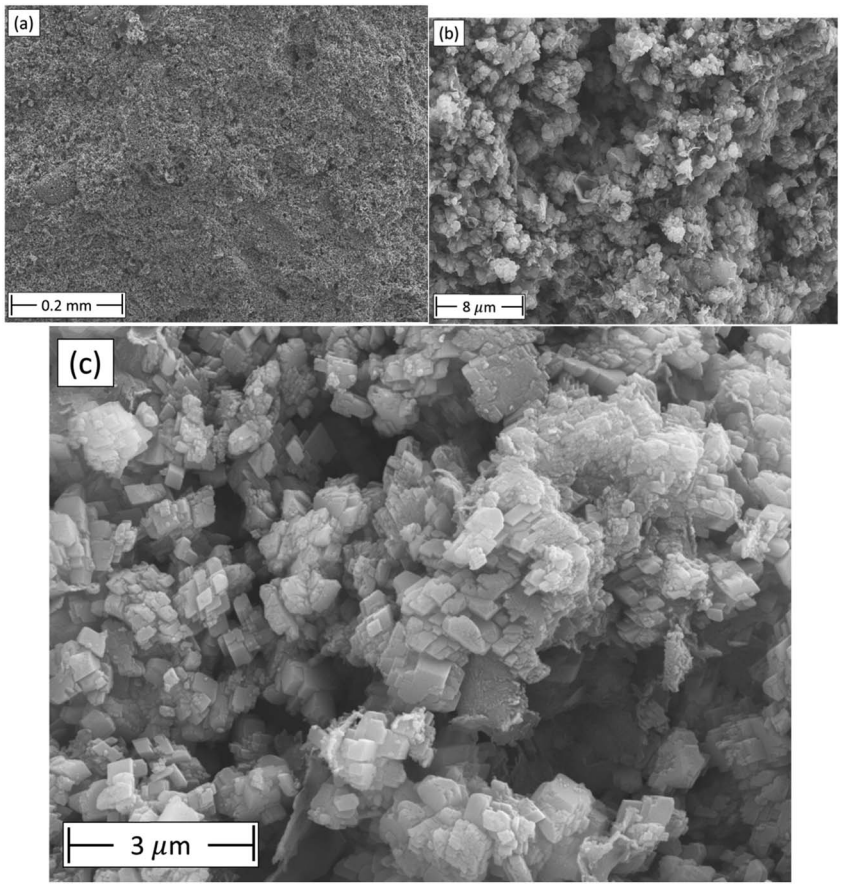

Figure 11. Microstructure of slice 5 of the tested core. Scale bare shown in each image. Complete reworking of the microstructure. Widths are (a) 3580, (b) 37, and (c) 8 μm, respectively.

core after the test is nonuniform, even though the test was performed at hydrostatic conditions. More radial compaction can be observed on the inlet side compared to the outlet side, indicating that the nonequilibrium of the injected fluids is more active here. This observation supports the idea that chemical interplay drives volumetric deformation.

4.5. Structural Reworking of the Microstructure Analyzed With SEM-EDS

In Table 5, it has been shown that compaction at 10.4 MPa (approximately 30% above yield) and flow of $MgCl_2$ brine induced significant changes in solid volume and pore volume. The focus here is on the microscopic structure of the grains. The scanning electron microscope (SEM) at the University of Stavanger (Norway) was used to image the microstructure morphology from untested slices of the core (Figure 9). The spatial variability on the microstructural morphology is large, as heterogeneities can be observed on a variety of scales. In Figure 9a, large-scale (i.e., 100 μm) voids (foraminifers) are observed to the left side. In Figures 9b–9d, SEM images from the untested end pieces of the Liège chalk can be seen at different magnifications. The calcium carbonate is found as intact or fragments of coccoliths together with rounded 0.5–2 μm grains. In addition, silicates can be seen as needles and sheets.

The untested core material from the end slices can be compared to tested samples from slices 2 and 5. Figure 10 displays three selected images with three different magnifications from slice 2 and similarly for slice 5 in Figure 11. In Figures 11a and 10a, no large-scale (100 μm) voids are observed indicating that larger-scale voids in the chalk have compacted [*Japsen et al.,* 2011]. Figures 10b, 10c, 11b, and 11c display that the microscopic morphology of the tested core material is completely changed compared to the untested material in Figures 9b–9d. The foraminifers and coccolith structures are less visible which indicates complete reworking of the microstructural morphology. This reworking affects the total mineral volume of the core. Some differences can be observed between slices 2 and 5.

Table 7. Overview of the Mass Transport Based on Estimates Before and After Experiment[a]

	Amounts in Concentration, Gram, and Mole With Upper and Lower Limits
Initial amount of $CaCO_3$	93.0 ± 2.0%, 116.8 ± 2.5 g, and 1.17 ± 0.03 mol
Initial amount of Ca	46.76 ± 1.0 g, 1.17 ± 0.03 mol
Initial non-carbonate content	8.79 ± 2.51 g
Produced Ca (IC, equation (16))	44.7 g and 1.12 mol
Amount of Ca left in core	2.06 ± 1.01 g and 0.08 ± 0.04 mol
Final retained Mg (from stoichiometry)	27.2 g and 1.12 mol
Final retained Mg (IC, equation (16))	31.3 g and 1.28 mol
Estimated mass loss	44.7–27.1 g = 17.6 g (stoichiometry argument for Mg) 44.7–31.28 g = 13.42 g (IC measurement of Mg)
Measured mass loss (on scale)	22.93 g
Non-carbonate mass loss (mass loss on scale minus the Mg-Ca exchange)	22.93–13.42 = 9.51 g (from IC) 22.93–17.58 = 5.34 g (from stoichiometry)
Mass correction factor, IC measurement (Γ)	$^{22.93}/_{13.42} = 1.71$

[a]The initial values of calcium carbonate contents are collected from *Zimmermann et al.* [2015], *Megawati et al.* [2012], and *Hjuler and Fabricius* [2009].

5. Discussion

Geochemical calculations performed using the techniques described in *Hiorth et al.* [2010], *Madland et al.* [2011], and *Cathles* [2006] show that several magnesium-bearing minerals, such as dolomite, magnesite, huntite, and brucite, are supersaturated when 0.219 *M* $MgCl_2$ is flooded through a chalk core at 130°C. When dissolution of the preexisting quartz inside the core is taken into account, the geochemical calculations show that several magnesium-bearing silicates, such as tremolite and talc, also may form. Dolomitization processes during Mg flow has been presented in reservoir chalk settings by, e.g., *Davies* [1979], *Davies and Smith* [2006], and *Smith and Davies* [2006]. The formation of anhydrite cement in addition to the dolomitization process impacting the porosity and flow pattern has been reported by, e.g., *Jones and Xiao* [2005] and *Al-Helal et al.* [2012]. The geochemical calculations above do not rule out that pressure solution at the grain contacts may give rise to additional dissolution and, farther down the line, reprecipitation of Mg (and/or Ca)-bearing minerals. However, this paper focuses on the measured chemical changes to the effluent water, potentially arising from multiple chemical processes (including pressure solution) and how these changes manifest themselves in the Darcy-scale quantities, such as permeability, porosity, and strain evolution.

The solid mass was reduced from 125.57 to 102.64 g, the solid volume was reduced from 46.85 cm^3 to 35.5 ± 0.1 cm^3. At the same time, the density increased from 2.69 to 2.90 g/cm^3 throughout the test period. The measurements of the pycnometer (solid volume), the pore volume measurement from the mass difference between the saturated and dry mass, and the total external volume are in line and show the same result in Table 5. After 1072 days of creep, the porosity is reduced from 41.32% to 40.14%, despite 25.81% volumetric strain. The low calcium effluent production during the last hundred days indicates that a complete chemical reworking of the chalk core occurred. This was confirmed by SEM images in Figures 9–11. In Table 7, we extracted some available data on the chemical constituency of Liège chalk from three recent studies. Based on these data, the plug consisted of ~1.17 ± 0.03 mol calcium before testing. By adding up the produced Ca ions through the effluent, we find that 1.12 mol is produced; thus, 93–98% of the initial Ca is produced from the core during the 1072 days of experiment.

At the same time, 1.28 mol of Mg is retained within the core. If only magnesite (or dolomite $CaMg(CO_3)_2$) was formed, there should be a one to one match (on a mole basis) of the magnesium loss and calcium gain. However, the ion chromatography (IC) results indicate a mismatch of 0.16 mol between the produced Ca and retained Mg, which can be related to the formation of other mineral phases as indicated above (e.g., brucite, tremolite, and/or talc). A correct geochemical explanation of the rock-fluid interactions has to take into account the discrepancy between the total weight loss of 22.93 g (measured on the scale) and the estimated 13.42 g weight loss from the IC data, i.e., the difference of 9.51 g (Table 7). Errors are always associated with the IC measurements. However, a mass given solely by Mg-Ca stoichiometric ion replacement is inadequate, because (a) the initial dry weight was 125 g, which corresponds to 1.17 mol of calcium carbonate for a 93% pure chalk. (b) If all Ca dissolved equals to 45.0 g and if Ca was replaced by Mg precipitation, it would add up

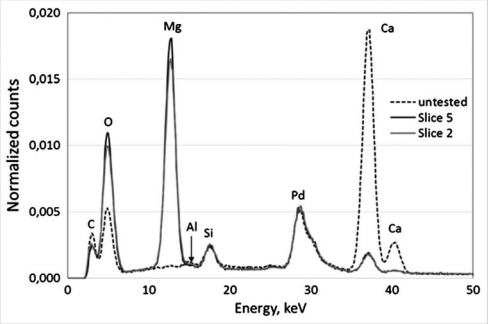

Figure 12. Rescaled EDS spectrum (normalized by the total number of counts). Slices 2 and 5 are compared to untested Liège chalk material (end slice from the trimming procedure before test). Each EDS plot represents an average of three scans. Note how Al and Si are unchanged; Ca is depleted, while O and Mg are increased compared to the untested material.

to 27.0 g, thus a mass loss of 18.0 g. This is the absolute theoretical upper limit of the mass loss related to Ca-Mg exchange. The difference between 18.0 g and the measured 22.93 g mass loss is significant compared to the scale measurement error (0.05 g for measurements above 100 g).

As is observed in the EDS spectra, the aluminum and silicate content remains unchanged (Figure 12) during the experiment. Thus, the gap between the measured mass loss and the estimated mass loss from the IC data cannot be associated with the 8.8 ± 2.5 g of noncarbonates that were present within the core before the experiment. Alternatively, it has been suggested that the mass discrepancy was associated with the production of fines. We find the production of fines to be unlikely, since the IC measurements account for more than 93% of the original Ca in the plug (1.12 of the 1.17 mol originally). The changes in mass, and the constituency of mass, led to considerable changes in the volume and density of the plug (Table 5). The search of an explanation to the observed mass loss finally pointed to production of carbonate ions from the core. If so, the 9.5 g discrepancy between the measured and IC-estimated mass loss indicates that 0.15 mol of carbonates (CO_3^{2-}) is produced from the core. Now the injected $MgCl_2$ brine is acidic with a pH of 5.6. Low pH (below 7) increases calcium solubility, thereby leading to enhanced dissolution. In the aqueous phase, carbonates and water form bicarbonate and hydroxide ($CO_3^{2-} + H_20 \rightarrow HCO_3^- + OH^-$). The increased concentration of OH^- ions in the produced water will act as a base increasing the pH of the effluent water. This is supported by the pH measurements in Figure 5. However, the pH measurement cannot be used directly since the water sampling was performed at atmospheric pressure and temperature conditions, leading to degassing of the dissolved CO_2 in the solution, and it is known that the CO_2 concentration also affects the pH level. To understand the measurements of the aqueous phase, rock-fluid models must be run to back calculate the pH within the core and to estimate the pH in the sample glass. In total, 72 L $MgCl_2$ brine was flushed through the sample. This led to significant mass loss (22.9 g), which could not be explained by changes in the noncarbonate content. IC measurements indicate that Mg and Ca accounts for 13.4 g, ~60% of the observed mass loss and the rest to the dissolution of carbonates (9.5 g, i.e., 0.16 mol). The discrepancy between the 1.12 mol Ca produced from the core and the 1.28 mol Mg retained in the core indicates that magnesium-bearing minerals reacting with the silicates and aluminum, such as tremolite and talc, have formed within the core. The exact nature of the observed mass loss requires more detailed analysis of the minerals in the core before and after testing, with the use of advanced analytical tools such as Mineral liberation analyses (MLA), X-ray diffraction (XRD), and nano-secondary ion mass spectrometry (nanoSims), which are out of scope of this paper.

EDS analyses provide semiquantitative measurements of the element concentration in the chalk. Three EDS scans were acquired from untested material from each end of the core and from slices 2 and 5 of the tested core material (i.e., in total, nine scans were performed). To ensure comparison between tested and untested material and along the flow direction, the scans were performed with the same field of view (190 μm horizontally). The samples were treated with palladium before they were mounted into the SEM-EDS machine. Each scan provided an EDS spectrum with counts along the *y* axis and energy (in keV) along the *x* axis. For comparison, the *y* axis was rescaled by the total number of counts and shown in Figure 12. The peaks in the EDS spectrum are identified as carbon, oxygen, magnesium, aluminum, silicate, palladium, and calcium.

5.1. Total, Solid, and Pore Volume Development

The bulk volume is given by the solid volume plus the void volume. While the porosity is given by the fraction of the pore volume by the bulk volume, the dynamic porosity evolution is given by the combined effect of bulk volumetric strain and changes to the solid volume. Rock-fluid chemistry interacts with the solid volume in multiple ways [*Ruiz-Agudo et al.,* 2014]. In the presented experiment, it is believed that solid

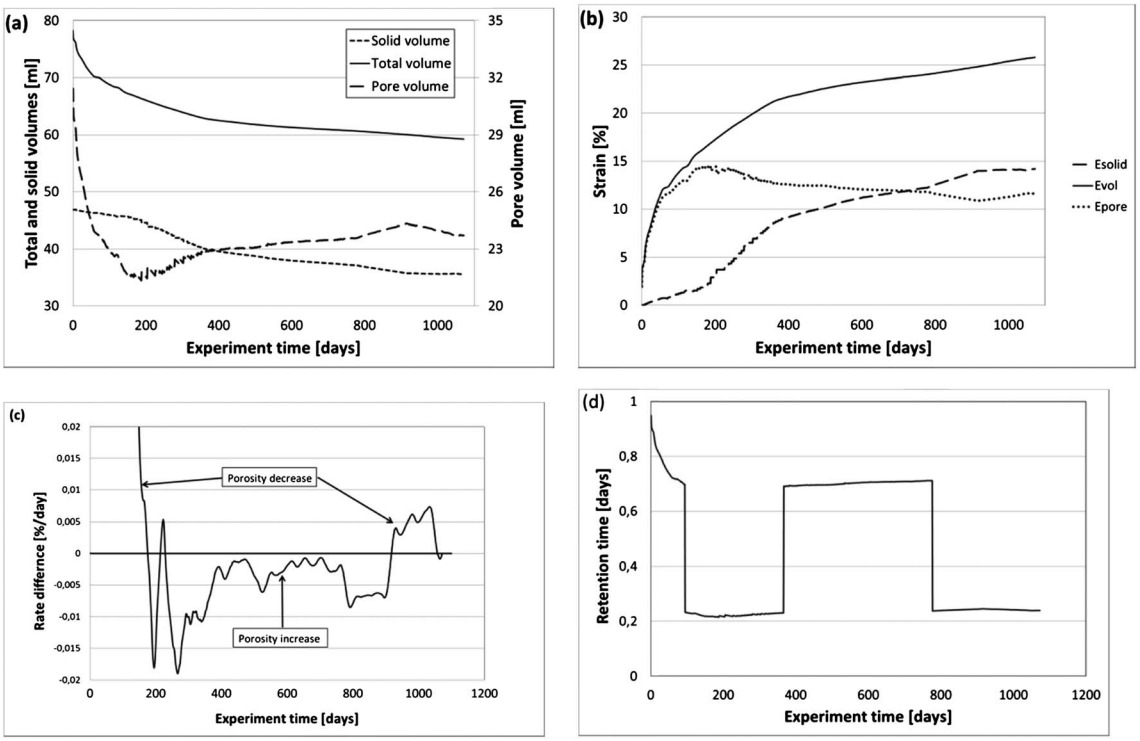

Figure 13. (a) Total bulk volume (black line), and solid volume over time (dotted line). Dotted line shows the pore volume from the difference in bulk and solid volume. (b) Bulk volumetric strain (solid line) and the chemical induced strain (dashed) calculated from equation (26). (c) Difference between rate of bulk volumetric strain and solid volumetric strain over time (time derivatives of the curves in Figure 13b). (d) Transport time for a fluid particle within the core.

volume changes are caused by calcium carbonate dissolution and precipitation of new secondary minerals and that solid volume-preserving mechanisms such as solid diffusion of chemical species are not dominating the chemical interplay.

In the average analysis of the grain pack, the solid volume development is given by the ratio of the mass evolution, divided by the density. To the first order, the mass evolution may be estimated from the Mg-Ca ion concentrations, even though the IC data can explain only 60% of the measured weight loss (13.42 g versus 22.93 g). We provide two ways forward by (a) merely using the IC data to the solid volume estimate (see, e.g., the porosity evolution in Figure 14) and (b) introducing a weight correction factor Γ that is assumed constant throughout the experiment. As such, the dry mass can be estimated. Furthermore, the density is assumed to evolve proportionally to the produced calcium between the limits of 2.69 and 2.90 g/cm^3 (pycnometer measurement before and after testing). In combination, these assumptions enable explaining the evolution of the bulk volume and solid volume in Figure 13a. An alternative approach to estimating the solid volume could be to use, e.g., titration measurements to obtain independent information of the pore volume, and thus the solid volume evolution, if the total volume is known. Even though the total volume steadily declines, the pore volume increases from ~200 days. In addition, the solid strain rate increases for increasing flow rate. As discussed around equation (23), the porosity development changes according to the two competing mechanisms, the bulk volume and solid volume development. In Figure 13c, the volumetric strain rate and the solid volumes are compared. For values above 0, the porosity decreases (as it does from 0 to 200 days and after 900 days when compaction is more rapid than chemical dissolution). Between 200 and 900 days, however, the value is negative indicating that the porosity increases. In Figure 13d, the retention time, given by the ratio of the pore volume by the injection rate of the fluid, was plotted over time.

5.2. Strain Partitioning

The observed volumetric strain can in its simplest form be partitioned into a chemical and mechanical component to understand how the observed volumetric strain develops over time during chemomechanical compaction. In the case where the chemical effects are related to dissolution and

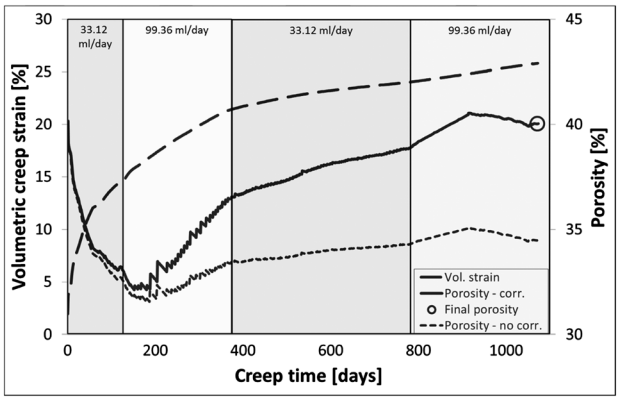

Figure 14. Plot of the volumetric strain (dashed line) and porosity with mass correction (solid line) and porosity without mass correction (dotted line). The volumetric strain is estimated from the axial strain with the correction factor ξ and the porosity according to equation (25) where the solid volume evolution (from mass and density from IC data) and total strain are included. The circle represents the measured porosity after test.

precipitation, we suggest linking the chemical strain to the evolution in the solid volume and the mechanical component related to the pore volume development:

$$\varepsilon_{\text{tot}} = \varepsilon_{\text{chem}} + \varepsilon_{\text{mech}} = \frac{\Delta V_s}{V_{b,0}} + \frac{\Delta V_p}{V_{b,0}} = \frac{\Delta V_b}{V_{b,0}} \tag{26}$$

The total observed volumetric strain and the solid volume strain are plotted in Figure 13b. The pore volume strain is the difference between the total bulk volume and solid volume. Here the volumetric creep strain is large in the beginning, with a steadily decreasing rate, while the dissolution rate depends on the flow rate until almost all of the initial calcium is produced from the plug.

5.3. Porosity

The pore volume is the difference between bulk volume and solid volume. Equivalently, we can estimate the porosity according to equation (25), where the solid volume and total volume development are included. In Figure 14, the porosity evolution and volumetric strain are plotted over time. The circle represents the measured porosity after the test. We see that the porosity decreases over time, until ~190 days, after which the porosity increases. This analysis displays how compaction by pore collapse competes with solid volume effects leading to either increasing or reducing porosity. Even though the bulk volume is reduced over time, the nonequilibrium nature of the rock-fluid interface ensures that the porosity evolves differently than what is expected from estimates using strain measurements alone. The mechanical component of compaction, related to pore volume reduction, evolves at a steadily declining rate while the dissolution rate is more or less constant if there is adequate calcium left in the core and the flow rate is constant. At the end of the experiment, 1.12 of the initial 1.17 mol of calcium is produced from the core, reducing the chemically induced porosity development toward the end of the experiment. This leads to a reducing porosity from 900 days.

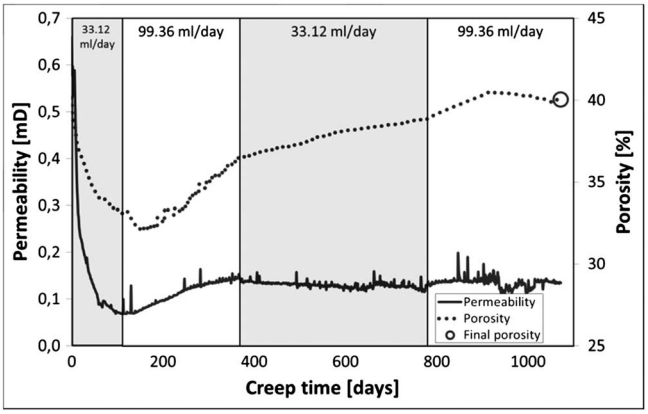

Figure 15. Plot of permeability and porosity. The measured permeability and estimated porosity is reduced during the first 100–150 days. Permeability and porosity increase when the estimated solid volume reduction rate is larger than the measured bulk volume reduction rate (Figure 13c). We interpret the shift from a decreasing to increasing permeability and porosity to be caused by the shift from when volumetric compaction dominates to dissolution dominates the observed dynamics. From 900 to 1072 days, the porosity decreases, as the volumetric compaction prevails while dissolution stops—since the remaining calcium carbonate contents in the core are limited.

5.4. Abnormal Permeability Evolution

In Figure 15, the permeability and the estimated porosity are displayed simultaneously. During the first 112 days, the permeability is reduced from ~0.6 to 0.1 mdarcy. During the same period of time, the porosity is reduced from 40% to ~30%. After approximately 140–160 days, the measured permeability starts increasing with time, which indicates that dissolution rather than compaction dominates the observed permeability dynamics. Assuming an inherent link

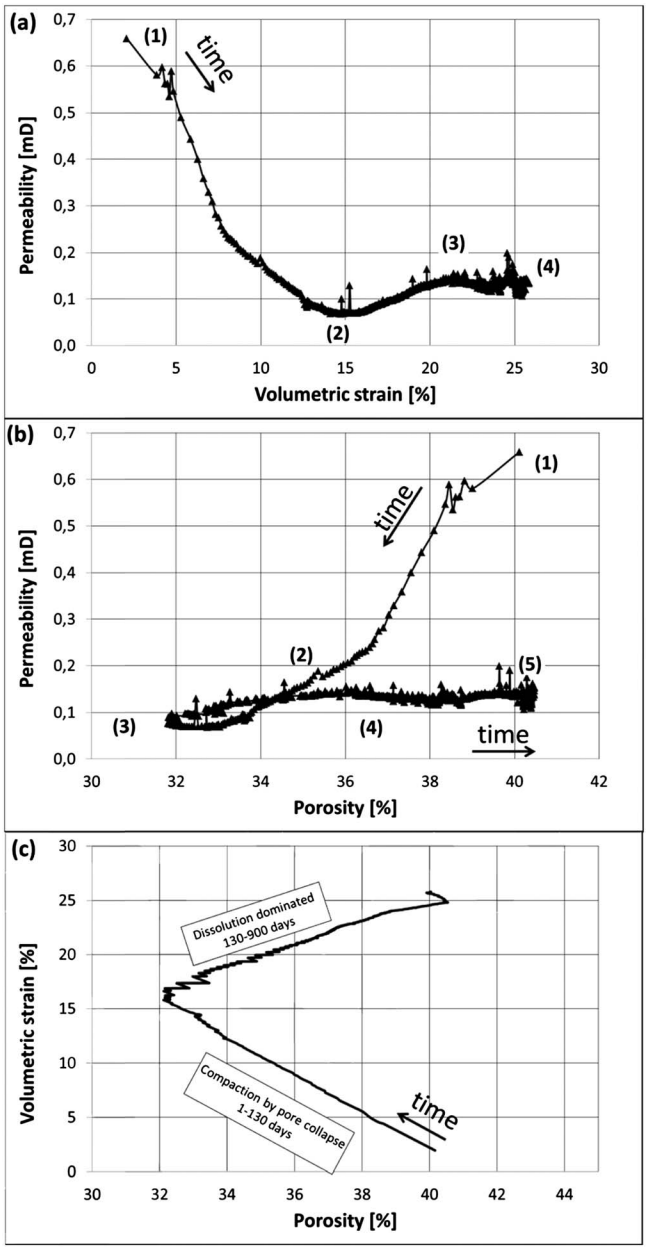

Figure 16. (a) Permeability as a function of volumetric strain 1 at start, 2 at 142 days, 3 at 400 days, and 4 at 1072 days. The permeability is reduced from 1 to 2 as the core compacts. This shifts from 2 to 4 in which the permeability increases despite the core compacts (and dissolves). (b) Measured permeability as a function of estimated porosity throughout the experiment. The numerals 1–5 represent the start, 35 days, 142 days, 550 days, and 1072 days. The permeability and porosity are reduced from 1 to 3, while the permeability increases and stabilizes as the porosity increases from 3 to 5. (c) Measured volumetric strain as a function porosity estimate.

between the permeability and porosity, the presented porosity model is more or less capable of predicting the transition from compaction-dominated to dissolution-dominated permeability dynamics. We can understand how a compaction-dominated process to a dissolution-dominated process affects the strain, since the rates of mechanical compaction by pore collapse reduce over time as the pore volume is reduced, while the chemical alteration is affected by the amount of reactive minerals that are flooded into the core. Most of the initial Ca was produced in the last 100 days, such that compaction dominates the porosity evolution.

When the flow rate was decreased to 33.12 cm^3/d at 378 days, the permeability stabilized at a plateau. We believe that the discrepancy in the increasing porosity evolution and stable permeability is associated with the formation of secondary minerals with a larger specific surface area.

5.5. Phase Plots

It is important to fully utilize all available data simultaneously, to learn some general lessons from the observed dynamics. One way to do this is to plot measurements and estimates against each other in phase plots. In Figure 16a, the measured permeability is plotted versus the measured volumetric strain. Point 1 represents the start of the creep phase and point 2 after 142 days. In this time period, the dynamics are dominated by compaction, and pore volume decreases. From points 2 to 3 at 400 days, the permeability increases even though the plug is still compacting. This period of time was dominated by dissolution, rather than compaction, as the injected flow rate was set to 99 cm^3/d. From points 3 to 4, the permeability remains more or less constant, which may indicate that the dissolution rate and compaction rates are comparable. In Figure 16b, the measured permeability is plotted together with the estimated porosity. This plot visualizes that during chemomechanical compaction of chalk permeability, relations that only include porosity dynamics are inadequate to capture the permeability development, i.e., the observed functional between the two parameters are not one to one. In Figure 16c, the volumetric strain is plotted against the estimated porosity, visualizing how the rate of

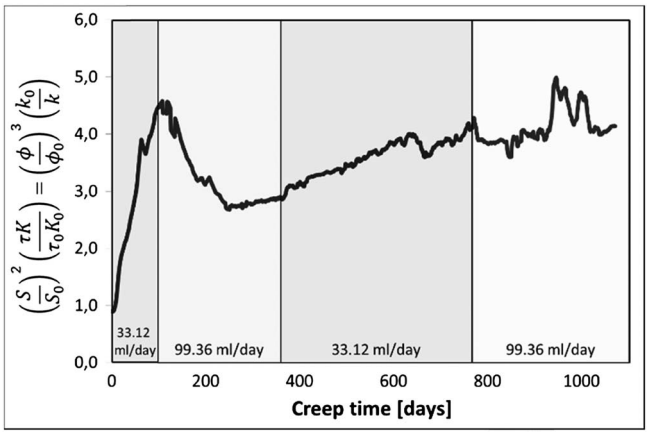

Figure 17. Plot of the rescaled porosity (to power 3) divided by the rescaled permeability enables the estimate of the specific surface area, tortuosity, and the Kozeny constant (equation (28)). The rescaled value increases to 4.57 after 112 days. After 112 days, the fluid injection rate increased by a factor of 3 and the dissolution increases which reduces the rescaled factor $\frac{S^2}{S_0^2}\frac{\tau K}{\tau_0 K_0}$ until 350 days. After ~350 days, the rescaling factor increases toward the end of the experiment.

chemical alteration of the solid volume and bulk compaction rate may dominate in various cases. Dissolution dominates the observed behavior when the compaction rate is low and the flow rate is high (increasing dissolution). On the other hand, compaction dominates for low flow rates and high compaction rates, leading to different dynamics in porosity, permeability, and compaction in different physical limits.

5.6. Hydraulic Permeability Models

Several permeability models have been presented in scientific literature in which the different models include several evolving parameters. The most frequently used parameters include the specific surface area (S), i.e., the total area the fluids have to pass, measured as either area per gram or area per volume; the tortuosity which describes the travel distance of a fluid particle divided by the Euclidean distance between two points ($\tau = l_p/l$); and the porosity which describes the volume in which fluids flow. The specific surface area can be estimated through adsorption experiments using the Brunauer-Emmett-Teller (BET) theory isotherm, and the tortuosity can be measured in specially designed experiments [see, e.g., *Matyka and Koza*, 2012]. Additional physical effects which affect the hydraulic permeability include granular morphology, grain angularity, packing structure, and widths of pore throats and pore bodies among others. Here the "sum" of these effects is incorporated into the Kozeny constant (K). In the following, we will employ the Carman-Kozeny model [*Feder*, 1996] in which the permeability is calculated from

$$k = \frac{\phi^3}{S^2 \tau K} \tag{27}$$

Changes to any of these variables induce changes to the permeability. In the presented experiment, we estimate changes in porosity and measure the changes in permeability. Rearranging equation (27) and rescaling the values with the initial values enable insight into the time evolution in the group of unconstrained parameters consisting of specific surface area, tortuosity, and Kozeny constant:

$$\left(\frac{S}{S_0}\right)^2\left(\frac{\tau K}{\tau_0 K_0}\right) = \left(\frac{\phi}{\phi_0}\right)^3\left(\frac{k_0}{k}\right) \tag{28}$$

The group of parameters is plotted in Figure 17 from the dynamic evolution in permeability and porosity showing an increase from 1, initially, to 4.6 at 112 days. From *Zimmermann et al.* [2015], where they present a similar $MgCl_2$ flooding experiment, it was shown that the specific surface area doubled, which increases the rescaled group by approximately a factor of 4. If the doubling in a specific surface area applies to the presented case, it explains the evolution of the right-hand side of equation (28). An observation can be noted in Figure 17. The rescaled factor is sensitive to the flow rate. From 0 to 112 days, the effluent analysis and volumetric strain indicate that the dominant mechanism is volumetric compaction by pore volume reduction. It is possible to envision that in a compaction-dominated process, whereby pore collapse and grain reorganization occur, new grain surfaces can be formed, or alternatively that new contact surfaces in between coccolith grains can be exposed to the flooding fluid and thereby effectively increasing the specific surface area. In addition, the area to volume ratio is higher for smaller grains. Any dissolution of smaller grains could explain the reduction in the squared specific surface area from 4.57 at a maximum to 2.81 at a minimum during the time from 112 to 210 days. From 300 days and toward the end of the experiment, the evolution in the specific surface evolves more or less linearly over time, until a doubling in the specific surface area is achieved at the end compared to that of the initial value.

5.7. The Formation of Dolomite and Magnesite During Flow of Mg-Rich Brines

It is of general interest to understand how the flow of Mg-rich brines affects the porosity evolution in carbonates. For example, in *Ehrenberg et al.* [2012], it is claimed that dissolution of carbonate rocks is insignificant due to the lack of empirical data in Earth systems and the fluid mass required to significantly alter the observed porosity. At the same time, dolomite ($CaMg(CO_3)_2$) is a mineral commonly observed in ancient carbonate rocks, in which calcium is replaced by magnesium during dissolution, precipitation, and compaction. Reviews on the topic of dolomitization [e.g., *Machel*, 2004; *Davies*, 1979; *Davies and Smith*, 2006; *Smith and Davies*, 2006], geological case studies of dolomitization processes taking chemistry and advection into account [e.g., *Consonni et al.,* 2010; *Al-Helal et al.,* 2012], and high-temperature experiments where calcite is dolomitized by Mg-Ca-Cl solutions with varying Mg/Ca ratios are abundant [see e.g., *Kaczmarek and Sibley,* 2011; *Montez-Hernandez et al.,* 2014]. In our system, we inject pure $MgCl_2$ brine, but due to the acidity, this induces dissolution of the calcite such that, effectively, Mg-Ca-Cl-CO_3 solution is formed in addition to the noncarbonate elements, such as silica and aluminum. Since more than 93% of the initial Ca has been produced from the core, it is likely that magnesite, instead of dolomite, has formed within the core. These observations are supported by the specific gravity measurements of the tested core material (2.90 ± 0.01 g/cm^3), which is larger than the specific gravity of dolomite (2.84–2.86 g/cm^3), while magnesite has a specific gravity of 3.00–3.10 g/cm^3. Since the specific gravity increased, this reduced the specific volume of the precipitated minerals. In addition, the fact that most of the initial Ca was produced from the plug, and the microscopic morphology of the grains changed, indicates that the formation of Mg-rich surface layers coating the chalk grains, as, e.g., described in *Ruiz-Agudo et al.* [2014], does not occur. Unanswered questions regarding the exact nature of fluid and the transport of ions across the grain boundary during dissolution and re-precipitation remain.

5.8. On the Simplifying Assumptions: The Correction Factor ξ and Γ and Homogenous Deformation

The axial to volume correction factor ξ was assumed constant throughout the experiment. In addition, it was assumed that the axial strain and chemical alteration were distributed homogeneously throughout the plug. Moreover, the simplifying assumption was made that the gap between the calculated mass evolution from the ion composition, and the measured weight of the plug could be bridged by the correction factor Γ. The average density of the solid phase was measured before and after the test, and it was assumed that the density at any given time was proportional to the produced calcium. With these assumptions, average properties for volumetric strain, evolution in mass and density (solid volume), and hence the porosity could be estimated with time.

It is acknowledged that the assumption of homogeneous deformation is a simplification, as the measured diameters along the plug after the test were nonuniform (Table 6 and Figure 7). The diameter was smaller at the center compared to the end pieces, and the diameter was smaller at the inlet side compared to the outlet side. The nonuniform radial strain indicates that nonzero shear forces were introduced and that chemical effects of the injected fluid occurred nonhomogenously throughout the plug (more intense chemical reworking at the inlet side). It is likely that dissolution is most prominent in the first couple of centimeters compared to downstream (at least in the first hundreds of days). The nonhomogeneity of the volumetric strain and chemical interaction violates the assumption of constant and uniform conversion factors ξ and Γ, although the assumption of average values fits on the whole core level.

Geochemical analysis of the plug will be presented in a forthcoming publication focusing on where, in what form, and to which degree the chemical alteration occurs along the core. Here we have presented an analysis that is in line with the available data, although it can easily extend to take into account, e.g., spatial variation if these observations are at hand.

6. Conclusions

We have presented a long-term chemomechanical compaction experiment with nonequilibrium water flooding lasting for 1072 days. During the test, we report measurements of the volumetric strain, the ion concentration, and pH of the effluent water samples, as well as the hydraulic permeability. Clearly, there are large mineralogical alterations inside the core. However, these investigations and the interpretation are a topic for a future paper.

In the data analyses, quite intriguing effects were displayed. The porosity is a dynamically evolving parameter controlled by the rate of compaction and the rate of chemical dissolution and precipitation. We saw that during the first 112–140 days, the dominating mechanism was compaction, leading to a steadily decline in the permeability. When the injection rate was increased by a factor of 3, dissolution became more important. Simultaneously, the volumetric creep rate decreased with time, thereby changing the dynamics from a compaction-dominated toward dissolution-dominated behavior. This was reflected in the increasing permeability development during 140–400 days. From 400 days, the injection rate was reduced. This led to reductions in the solid volume evolution rate, approaching the total volume evolution rate, thus leading to a reduced rate of porosity increase. When practically all the Ca is produced from the plug at 900 days, the solid volume evolution rate approaches 0. At the same time, the plug is still compacting slightly, which leads to a period of porosity decrease toward the end of the experiment. At the end of the experiment, the porosity had changed from 41.32% to 40.02% despite the plug accommodating more than 25% (volumetric strain). This exemplifies how dissolution and precipitation of the solid volume may significantly alter the porosity evolution during compaction. Generally in reactive systems, the evolution in porosity depends on the rates of the pore volume evolution and solid volume evolution dynamics.

The solid density changed from 2.68 to 2.90 g/cm^3 throughout the experiment. At the same time, the core had lost 22.93 g. The estimated solid volume loss from the ratio of mass divided by density changes was in line with the solid volume estimates obtained from the saturated and dry weight measurements after the experiments. Thus, it is safe to conclude that solid volume changes occur during flooding of $MgCl_2$ brines. Accounting for changes in the total volume and solid volume, we developed an equation for the porosity dynamics. The proposed porosity evolution equation is in line with the independently measured permeability development, giving the porosity evolution equation some confidence. The porosity evolution equation incorporates the combined effects of

1. dissolution which contributes to an increase in porosity if everything else is equal;
2. precipitation of secondary minerals within the pore volumes leading to a decrease in porosity if everything else is equal; and
3. bulk volumetric compaction which leads to a porosity decrease if everything else is equal.

We believe that permeability models add valuable insight into the observed dynamics in these experiments. Evaluating permeability models may shed light onto the other parameters of interests, such as the specific surface area. We believe that we have presented a novel approach to the analysis of compaction and fluid-rock core-scale experiments and that the utilization of permeability-porosity models paves the way for further insight into the dynamics of, e.g., experimental diagenesis. Improvements may be made upon more correct solid density evolution curves, from, e.g., geochemical models. In addition, if there were direct ways of measuring the specific surface area and tortuosity through time, we could improve the search for more accurate empirical functions for permeability, which is of great importance to estimate flow properties in hydrology and reservoir engineering.

Acknowledgments

The authors would like to thank the grant "Water weakening at in-situ conditions" from the Norwegian Research Council, Joint Chalk Research phase 7 (JCR-7) and the Valhall and Ekofisk co-venturers including BP Norge, Hess Norge AS, Total E&P Norge AS, ConocoPhilips, Statoil, Petoro, DONG Energy, Maersk Oil, Shell, and Nordsøfonden for their financial support. In addition, the authors acknowledge Siv Marie Åsen (IRIS), Mona Minde (IRIS/UiS for SEM-EDS), Vladimir Traskine (Moscow University), Yves Bernabe, and an anonymous reviewer for their fruitful contributions to the manuscript. The data for this paper are available by contacting the corresponding author.

References

Alam, M. M., I. Fabricius, and H. Christensen (2012), Static and dynamic effective stress coefficient of chalk, *Geophysics*, *77*(2), doi:10.1190/GEO2010-0414.1.

Al-Helal, A., F. Whitaker, and Y. Xiao (2012), Reactive transport modeling of brine reflux: Dolomitization, anhydrite precipitation and porosity evolution, *J. Sediment. Res.*, *82*, 196–215, doi:10.2110/jsr.2012.14.

Amyx, J., D. Bass Jr., and R. Whithing (1960), *Petroleum Reservoir Engineering*, McGraw-Hill Inc., New York.

Andrade, E. N., R. F. Randall, and M. Makin (1950), The Rehbinder effect, *Proc. Phys. Soc. London, Sect. B*, *63*, 990–995.

Awan, A., R. Teigland, and J. Kleppe (2008), *A Survey of North Sea Enhanced Oil Recovery Projects Initiated During the Years of 1975 to 2005*, SPE/DOE Enhanced Oil Recovery Symposium, pp. 497–512, SPE Reservoir Evaluation & Engineering, Tulsa, Okla.

Biot, M. (1941), General theory of three-dimensional consolidation, *J. Appl. Phys.*, *12*, 155–164, doi:10.1063/1.1712886.

Cathles, L. (1981), Fluid flow and genesis of hydrothermal ore deposits, *Econ. Geol.*, *75*, 424–457.

Cathles, L. (2006), *Eq-Alt-Equilibrium Chemical Alteration in Combined Physical and Chemical Geofluids Modeling*, Univ. of Windsor, Windsor, Ontario.

Charlez, P. (1991), *Rock Mechanics: Theoretical Fundamentals*, Editions Technip, Paris.

Consonni, A., P. Ronchi, C. Geloni, A. Battistelli, D. Grigo, S. Biagi, F. Gherardi, and G. Gianelli (2010), Application of numerical modelling to a case of compaction-driven dolomitization: A Jurassic palaeohigh in the Po Plain, Italy, *Sedimentology*, *57*, 209–231.

Croize, D., F. Renard, K. Bjørlykke, and D. Dysthe (2010), Experimental calcite dissolution under stress: Evolution of grain contact microstructure during pressure solution creep, *J. Geophys. Res.*, *115*, B09207, doi:10.1029/2010JB000869.

Croize, D., F. Rendard, and J.-P. Gratier (2013), Compaction and porosity reduction in carbonates: A review of observations, theory and experiments, *Adv. Geophys.*, *54*, 181–238.
Davies, G. (1979), AAPG short course on dolomite reservoir rocks: Processes, controls and porosity development (report), Calgary, Alberta, Canada: AAPG.
Davies, G., and L. Smith (2006), Structurally controlled hydrothermal dolomite reservoir facies: An overview, *AAPG Bull.*, *90*(11), 1641–1690.
Doornhof, D., T. G. Kristiansen, N. B. Nagel, P. D. Pattillo, and C. Sayers (2006), Compaction and subsidence, *Oilfield Rev.*, *50–68*.
Durand, J. (1997), *Sands, Powders and Grains - An Introduction to the Physics of Granular Materials*, Springer, New York.
Ehrenberg, S., O. Walderhaug, and K. Bjørlykke (2012), Carbonate porosity creation by mesogenetic dissolution: Reality or illusion?, *AAPG Bull.*, *96*(2), 217–233.
Emberley, S., I. Hutcheon, M. Shevalier, K. Durocher, B. Mayer, W. Gunter, and E. H. Perkins (2005), Monitoring fluid-rock interaction and CO_2 storage through produced fluid sampling at the Weyburn CO_2 injection enhanced oil recovery site, Saskatchewan, Canada, *Appl. Geochem.*, *20*, 1131–1157.
Engstrøm, F. (1992), Rock mechanical properties of Danish North Sea chalk, 4th North Sea chalk symposium.
Feder, J. (1996), *Flow in Porous Media*, Course material/Lecture Notes, Physics Dept. Univ. of Oslo, Oslo, Norway.
Fjær, E., R. Holt, P. Horsrud, A. Raaen, and R. Risnes (2008), *Petroleum Related Rock Mechanics*, 2nd ed., 491 pp., Elsevier, Amsterdam.
Grgic, D. (2011), Influence of CO_2 on the long-term chemomechanical behavior of oolitic limestone, *J. Geophys. Res.*, *116*, B07201, 1–21, doi:10.1029/2010JB008176.
Heggheim, T., M. Madland, R. Risnes, and T. Austad (2005), A chemical induced enhanced weakening of chalk by seawater, *J. Petrol. Sci. Eng.*, *46*, 171–184.
Hellmann, R., P. Gaviglio, P. Renders, J.-P. Gratier, S. Bèkri, and P. Adler (2002a), Experimental pressure solution compaction of chalk in aqueous solutions. Part 2. Deformation examined by SEM, posimetry, synthetic permeability, and X-ray computerized tomography, in *Water - Rock Interactions, Ore Deposits, and Environmental Geochemistry: A tribute to David A. Crerar*, edited by R. Hellmann and S. A. Woods, pp. 153–178, Geochemical Society.
Hellmann, R., P. Renders, J.-P. Gratier, and R. Guiguet (2002b), Experimental pressure solution compaction of chalk in aqueous solutions. Part 1. Deformation behavior and chemistry, in *Water Rock Interactions, Ore Deposits, and Environmental Geochemistry: A tribute to David A. Crerar*, edited by R. Hellmann and S. A. Wood, pp. 129–152, Geochemical Society.
Hermansen, H., L. Thomas, J. Sylte, and B. Aasboe (1997), Twenty five years of Ekofisk reservoir management, *Soc. Petrol. Eng.*, doi:10.2118/38927-MS.
Hermansen, H., G. Landa, J. Sylte, and L. Thomas (2000), Experiences after 10 years of waterflooding the Ekofisk Field, Norway, *J. Petrol. Sci. Eng.*, *26*(1–4), 11–18.
Hiorth, A., L. Cathles, and M. Madland (2010), The impact of pore water chemistry on carbonate surface charge and oil wettability, *Trans. Porous Media*, *85*(1), 1–21.
Hiorth, A., E. Jettestuen, J. Vinningland, L. Cathles, and M. Madland (2013), Thermo-chemistry reservoir simulation for better EOR prediction, Stavanger, Norway: IEA EOR 34th Annual Symposium.
Hjuler, M., and I. Fabricius (2009), Engineering properties of chalk related to diagenetic variations in the Upper Cretaceous onshore and offshore chalk in the North Sea Area, *J. Petrol. Sci. Eng.*, *68*, 151–170.
Japsen, P., D. Dysthe, E. Hartz, S. Stipp, V. Yarushina, and B. Jamtveit (2011), A compaction front in North Sea chalk, *J. Geophys. Res.*, *116*, B11208, doi:10.1029/2011JB008564.
Jensen, T., K. Harpole, and A. Østhus (2000), EOR screening for Ekofisk, Paris, France: SPE 65124.
Jones, G., and Y. Xiao (2005), Dolomitization, anhydrite cementation and porosity evolution in a reflux system: Insights from reactive transport models, *AAPG Bull.*, *89*(5), 577–601.
Kaczmarek, S., and D. Sibley (2011), On the evolution of dolomite stoichiometry and cation order during high-temperature synthesis experiments: An alternative model for the geochemical evolution of natural dolomites, *Sediment. Geol.*, *240*, 30–40.
Korsnes, R., M. Madland, T. Austad, S. Haver, and G. Røsland (2008a), The effects of temperature on the water weakening of chalk by seawater, *J. Petrol. Sci. Eng.*, *60*, 183–193.
Korsnes, R., E. Wersland, T. Austad, and M. Madland (2008b), Anisotropy in chalk studied by rock mechanics, *J. Petrol. Sc. Eng.*, *62*, 28–35.
Kristiansen, T., O. Barkved, K. Buer, and R. Bakke (2005), Production-induced deformations outside the reservoir and their impact on 4D seismic, International Petroleum Technology Conference.
Liteanu, E., and C. Spiers (2009), Influence of pore fluid salt content on compaction creep of calcite aggregates in the presence of supercritical CO_2, *Chem. Geol.*, *265*, 134–147.
Liteanu, E., C. Spiers, and J. de Bresser (2013), The influence of water and supercritical CO_2 on the failure behavior of chalk, *Tectonophysics*, *599*, 157–169.
Machel, H. (2004), Concepts and models of dolomitization: A critical reappraisal, *Geol. Soc., London Spec. Publ.*, *235*, 7–63.
Madland, M., R. Korsnes, and R. Risnes (2002), Temperature effects in Brazilian, uniaxial and triaxial compressive tests with high porosity chalks, 77761, pp. 1–11. San Antonio, USA: Society of Petroleum Engineers SPE Annual Technical Conference and Exhibition.
Madland, M., A. Finsnes, A. Alkafadgi, R. Risnes, and T. Austad (2006), The influence of CO_2 gas and carbonate water on the mechanical stability of chalk, *J. Petrol. Sci. Eng*, *51*, 149–168.
Madland, M., A. Hiorth, E. Omdal, M. Megawati, T. Hildebrand-Habel, R. Korsnes, S. Evje, and L. M. Cathles (2011), Chemical alterations induced by rock-fluid interactions when injecting brines in high porosity chalks, *Trans. Porous Media*, *87*(3), 679–702.
Matyka, M., and Z. Koza (2012), How to calculate tortuosity easily? arXiv: 1203.5646v1 [physics.flu-dyn], 1–6.
Megawati, M., A. Hiorth, and M. Madland (2012), The impact of surface charge on the mechanical behaviour of high-porosity chalk, *Rock Mech. Eng.*, doi:10.1007/s00603-012-0317-z.
Montez-Hernandez, G., N. Findling, F. Renard, and A.-L. Auzende (2014), Precipitation of ordered dolomite via simultaneous dissolution of calcite and magnesite: New experimental insights into an old precipitation enigma, *Cryst. Growth Des.*, *14*, 671–677, (ACS Publications).
Nagel, N. (2001), Compaction and subsidence issues within the petroleum industry: From Wilmington to Ekofisk and beyond, *Phys. Chem. Earth (A)*, *26*(1–2), 3–14.
Nermoen, A., R. Korsnes, H. Christensen, N. Trads, A. Hiorth, and M. Madland (2013), *Measuring the Biot Stress Coefficient and Its Implications on the Effective Stress Estimate*, pp. 13–282, ARMA, San Francisco, pp. 1–9, American Rock Mechanics Association.
Nermoen, A., R. Korsnes, S. Haug, A. Hiorth, and M. Madland (2014), The dynamic stability of chalks during flooding of nonequilibrium brines and CO_2, Stavanger: Fourth EAGE CO_2 Geological Storage Workshop, Demonstrating storage integrity and building confidence in CCS.
Neveux, L., D. Grgic, C. Carpentier, J. Pirnon, L. Truche, and J. Girard (2014a), Influence of hydrocarbon injection on the compaction by pressure solution of a carbonate rock: An experimental study under triaxial stresses, *Marine and Petroleum Geology*, *55*, 282–294.

Neveux, L., D. Grgic, C. Carpentier, J. Pironon, L. Truche, and J. Girard (2014b), Experimental simulation of chemomechanical processes during deep burial diagenesis of carbonate rocks, *J. Geophys. Res. Solid Earth*, *119*, 984–1007, doi:10.1002/2013JB010516.

Nur, A., and J. Byerlee (1971), An exact effective stress law for elastic deformation of rock with fluids, *J. Geophys. Res.*, *76*(26), 6414–6419, doi:10.1029/JB076i026p06414.

Omdal, E. (2010), *The Mechanical Behavior of Chalk Under Laboratory Conditions Simulating Reservoir Operations (Phd)*, Univ. of Stavanger, Stavanger, Norway.

Omdal, E., H. Breivik, K. Næss, T. Kristiansen, R. Korsnes, A. Hiorth, et al. (2009), Experimental investigation of the effective stress coefficient for various high-porosity outcrop chalks, Proc. of the 43rd US Rock Mechanics Symposium and the 4th US-Canada Rock Mechanics symposium, Asheville: ARMA 09-118.

Rehbinder, P., and E. Shchukin (1972), Surface phenomena in solids during deformation and fracture process, *Prog. Surf. Sci.*, *3* (pt. 2), 97–104.

Risnes, R. (2001), Deformation and yield in high porosity chalks, *Phys Chem Earth (A)*, *26*(1–2), 53–57.

Risnes, R., H. Haghighi, R. Korsnes, and O. Natvik (2003), Chalk-fluid interactions with glycol and brines, *Tectonophysics*, *370*, 213–226.

Risnes, R., M. Madland, M. Hole, and N. Kwabiah (2005), Water weakening of chalk - Mechanical effects of water-glycol mixtures, *J. Petrol. Sci. Eng.*, *48*, 21–36.

Røyne, A., J. Bisschop, and D. Dysthe (2011), Experimental investigation of surface energy and subcritical crack growth in calcite, *J. Geophys. Res.*, *116*, B04204, doi:10.1029/2010JB008033.

Ruiz-Agudo, E., C. Putnis, and A. Putnis (2014), Coupled dissolution and precipitation at mineral-fluid interfaces, *Chem. Geol.*, *383*, 132–146.

Shafer, J., K. Vorhaben, and G. Boitnott (2012), Large pressure depletions in ultra deepwater GOM reservoirs can significantly reduce near well bore permeability and pore volume, Aberdeen, Scotland, UK 27.–30. August: International Symposium of Core Analyst (SCA).

Smith, L., and G. Davies (2006), Structurally controlled hydrothermal alteration of carbonate reservoirs: Introduction, *AAPG Bull.*, *90*(11), 1635–1640.

Spencer, A. M., P. I. Briskeby, L. Dyrmose Christensen, R. Foyn, F. Kjølleberg, E. Kvadsheim, I. Knight, M. Rye-Larsen, and J. Williams (2008), Petroleum geoscience in Norden - Exploration, production and organization, *Episodes*, *31*(1), 115–124.

Terzaghi, K. (1923), Die berechnung der durchassgikeitsziffer des tones aus dem Verlauf der hydrodynamishen Spannungserscheinungen, *Sitzungsber. Akad. Wiss. Wien. Math-Naturwiss Kl. Abt*, *2A*(132), 105.

Traskin, V. (2009), Rehbinder effect in tectonophysics, *Phys. Solid Earth*, *45*(11), 952–963.

Vasquez, G., E. do Amaral Vargas Jr., C. Riberio, M. Leao, and J. Justen (2009), Experimental determination of the effective pressure coefficient for Brazilian limestones and sandstones, *Rev. Brasilieara Geofis.*, *27*(1), 43–53.

Zimmermann, U., et al. (2015), Evaluation of the compositional changes during flooding of reactive fluids using scanning electron microscopy, nano-secondary ion mass spectrometry, x-ray diffraction, and whole-rock geochemistry, *AAPG Bull.*, *99*(5), 791–805, doi:10.1306/12221412196.